

Sensitivity of Tropical Cyclone Intensity Variability to Different Stochastic Parameterization Methods

Mahashweta Patra¹, Wai-Tong Louis Fan^{2,3} and Chanh Kieu^{1,*}

¹Department of Earth and Atmospheric Sciences, Indiana University, Bloomington, IN 47405

²Department of Mathematics, Indiana University, Bloomington, IN 47405

³Center of Mathematical Sciences and Applications, Harvard University, Cambridge, MA 02138.

Correspondence*:

Chanh Kieu, Department of Earth and Atmospheric Sciences, Indiana University, Bloomington, IN 47405.

ckieu@indiana.edu

2 ABSTRACT

3 Proper representations of stochastic processes in tropical cyclone (TC) models are critical for
4 capturing TC intensity variability in real-time applications. In this study, three different stochastic
5 parameterization methods including random initial conditions, random parameters, and random
6 forcing are used to study TC intensity variation and uncertainties. Using a fidelity-reduced
7 dynamical model and a cloud-resolving model (CM1), it is shown that random forcing produces
8 the largest variability of TC intensity at the maximum intensity equilibrium and the fastest intensity
9 error growth during TC rapid intensification. In contrast, random initial condition tends to be more
10 effective during the early stage of TC development but becomes less significant at the mature
11 stage. For the random parameter method, it is found that this approach depends sensitively on
12 how the model parameters are randomized. Specifically, randomizing model parameters at the
13 initial time appears to produce much larger effects on TC intensity variability and error growth
14 as compared to randomizing model parameters every model time step, regardless of how large
15 the random noise amplitude is. These results suggest the importance of choosing a random
16 representation scheme to capture proper TC intensity variability in practical applications.

17 **Keywords:** Tropical cyclone development, Stochastic parameterization, Intensity error growth, Intensity error saturation, Random
18 representation.

1 INTRODUCTION

19 The application of stochastic physics parameterizations to weather and climate models is a rapidly advancing
20 and important topic in current modelling systems (Palmer (2001); Christensen et al. (2015); Dorrestijn
21 et al. (2015)). Palmer (2012) argued from both theoretical and practical bases that all comprehensive
22 weather and climate models, no matter how complex the models are, should be stochastic in nature. From
23 this perspective, although the governing equations are formally deterministic, the best predictions should
24 be based on models that could capture the uncertainty of the atmosphere, whether for climate on long
25 time scales or weather on time scales of days to weeks. Developing practical tools for estimating such

26 uncertainty of model forecasts would require the knowledge of random error effects, which then allows us
27 to investigate the relative impacts of different types of uncertainties in models.

28 In general, TC intensity forecast errors in any numerical model are caused by several factors including
29 model errors, vortex initial uncertainties, global boundary guidance errors, random environmental forcings,
30 or the intrinsic nature of TC intensity variability (Gopalakrishnan et al., 2011; Tallapragada et al., 2012;
31 Kieu et al., 2018; Halperin and Torn, 2018; Trabling and Bell, 2020; Kieu et al., 2021, NKF). While
32 these factors are technically non-separable in practice due to the nonlinear nature of TC dynamics and
33 thermodynamics, it is possible to examine their relative roles under some specific conditions. For example,
34 real-time verification of TC intensity forecast shows that model errors tend to be more important at the
35 longer lead time as compared to vortex initial condition errors (Du et al., 2013; Kieu et al., 2021). Likewise,
36 uncertainties in global lateral boundary conditions could result in a wrong track forecast, which can lead to
37 large intensity errors for incorrect landfalling storms or TCs under rapidly changing environments even in
38 perfect regional models with perfect initial conditions Kieu et al. (2021).

39 Among those sources of intensity errors, the impacts of different random types on TC intensity variability
40 appear to be the least examined. Even under the most idealized conditions with no other sources of model or
41 initial condition errors, the atmospheric random fluctuation always exists and introduces an uncontrollable
42 uncertainties into TC development. While these random fluctuations are often small and probably less
43 important than other types such as model or initial condition errors, the nonlinearity of TC dynamics could
44 amplify random fluctuations during TC development and eventually lead to noticeable variability in TC
45 intensity that is currently not fully understood.

46 Despite such an inherent random nature of the atmosphere, examining how it affects TC intensity,
47 especially the relative importance of different stochastic representations during TC intensification, is still
48 an open question due to various ways that random noise is parameterized in TC models. Using a low-order
49 TC model, (Nguyen et al., 2020, hereinafter NKF) recently examined the effects of random noise in
50 terms of the Wiener process at the maximum intensity equilibrium. By analyzing the invariant intensity
51 distribution at the mature stage, they showed that the stochastic forcing associated with tangential wind
52 and warm-core anomaly has the largest contribution to TC intensity variability. This theoretical result is
53 consistent with previous modelling studies, which captured strong sensitivity of TC intensity to vortex
54 initialization schemes and warm core retrieval in TC models (Kurihara et al., 1995; Van Nguyen and Chen,
55 2011; Rappin et al., 2013; Liu et al., 2000; Zou and Tian, 2018). How the effects of stochastic forcing are
56 compared to those caused by random parameters or vortex initial condition have not been addressed.

57 In this study, we wish to examine how different methods of representing atmospheric random noise will
58 affect the variability of TC intensity as well as the intensity error growth during TC rapid intensification.
59 Understanding the relative roles of stochastic parameterization approaches in TC intensity variability will
60 help quantify an intensity error limit that one can achieve with numerical models in the future. Likewise,
61 examining the error growth during the intensifying stage will help evaluate how the accuracy of TC intensity
62 forecast evolves during TC development for operational applications. For this purpose, we will use both a
63 fidelity-reduced TC model (Kieu, 2015; Kieu and Wang, 2017, hereinafter KW17) and the cloud-resolving
64 (CM1 Bryan and Fritsch (2002)) model to study the effectiveness of different stochastic representation
65 methods in capturing TC intensity fluctuations.

66 The structure of the paper is organized as follows. Section. 2.1 presents a brief introduction of the TC-
67 scale dynamical model, its extension for a stochastic system, and different types of random representations.
68 Section 2.2 discusses the application of the stochastic parameterization for the CM1 model. Detailed

69 algorithm to calculate the error growth during the rapid intensification are provided in Section 2.3. The
 70 results from the fidelity-reduced model are presented in Section 3, while error saturation at the mature
 71 stage and error growth for the CM1 model are discussed in Section 4. Finally, some concluding remarks
 72 are given in Section 5.

2 METHODOLOGY

73 2.1 Fidelity-reduced TC model

74 Given the complex nature of TC dynamics, a complete investigation of different stochastic mechanisms in
 75 full-physics TC models is generally not feasible. This is because full-physics models are highly nonlinear
 76 with various parameterization schemes that not only require a large computational resource to conduct
 77 stochastic simulations but also introduce insurmountable difficulty in analyzing nonlinear interactions
 78 among different physical components.

79 As a first step to examine the effects of different stochastic parameterizations on TC intensity, a simple
 80 model for TC development is needed. Among several existing low-order TC models, the TC-scale model
 81 proposed by Kieu (2015) and modified further by KW17 (hereinafter referred to as the modified TC-
 82 scale dynamics, or MSD, model) is of specific interest. Using TC scales as dynamical variables in the
 83 axisymmetric framework, the scale analyses of the governing equation can be reduced to a set of ordinary
 84 differential equations that contain only a few TC basic scales including the maximum tangential wind (v),
 85 the maximum radial wind at the surface (u), and the warm anomaly in the TC central region (b). With the
 86 wind-induced surface heat exchange feedback closure, these nondimensional scale equations are given as
 87 follows

$$\dot{u} = pv^2 - (p + 1)b - C_d u |v| \quad (1)$$

$$\dot{v} = -uv - C_d v |v| \quad (2)$$

$$\dot{b} = bu + su + T_s |v| - rb. \quad (3)$$

88 This MSD model includes several parameters (p, s, r, C_d, T_s) that characterize the TC dynamics, where p
 89 is a constant proportional to the squared ratio of the depth of the troposphere to the depth of the boundary
 90 layer, s denotes the effective tropospheric static stability, r represents the Newtonian cooling, and C_d and
 91 T_s are nondimensional parameters representing the surface drag coefficient and sea surface temperature
 92 (SST). Note that unlike the original MSD system in KW17 for which C_d and T_s are scaled to have a value
 93 1, we retain their explicit role in this study such that the sensitivity of TC intensity and the error growth to
 94 these parameters can be explored.

95 While the MSD model is simple, it has a number of properties that are attractive for our investigation of
 96 random representations in this study. First, this system is explicitly time-dependent, which is required to
 97 examine the evolution of TC intensity as well as related error growth during TC intensification. Second, the
 98 model contains the maximum potential intensity (MPI) limit as its unique stable point in the phase space of
 99 (u, v, b) as discussed in KW17. The existence of such a stable point is vital, because it allows us to quantify
 100 how the variability of TC intensity at the mature stage depends on different random parameterization
 101 methods as discussed in NKF.

102 While the MSD system could describe both cyclonic and anticyclonic flows as discussed in Kieu and
 103 Wang (2018), we will limit our consideration hereinafter to cyclonic TCs in the Northern Hemisphere

104 such that the absolute signs in Eqs. (1)-(3) can be removed. In the next subsections, we will describe
 105 three different random mechanisms and how to implement them for the MSD system. These mechanisms
 106 include i) random forcing, ii) random initial condition, and iii) random parameters, which are the most
 107 commonly-used methods in current numerical weather prediction models.

108 2.1.1 Random forcing (RF) representation

109 We examine first a type of random representation in which the model forcing is augmented by stochastic
 110 processes, often known also as physical stochastic parameterization (Palmer, 2001; Christensen et al., 2015;
 111 Dorrestijn et al., 2015). According to this method, random noise is added to prognostic variable tendencies
 112 or model states with different spatial and temporal scales (see, e.g., Palmer, 2001; Weisheimer et al., 2011;
 113 Zhang et al., 2015; Christensen, 2020). This approach is equivalent to adding random noise to model
 114 forcing as discussed in (NKF, Fan et al., 2021b), and will be hereinafter referred to as the random forcing
 115 (RF) method.

116 Following NKF, we introduce additive driving noise in terms of the Wiener process to the MSD system
 117 (1)-(3) and obtain the following stochastic differential equations

$$dU_t = (pV_t^2 - (p+1)B_t - C_dU_tV_t) dt + \sigma_u dW_t^{(u)} \quad (4)$$

$$dV_t = (-U_tV_t - C_dV_tV_t) dt + \sigma_v dW_t^{(v)} \quad (5)$$

$$dB_t = (B_tU_t + sU_t + T_sV_t - rB_t) dt + \sigma_b dW_t^{(b)}, \quad (6)$$

118 where $\{W^{(u)}, W^{(v)}, W^{(b)}\}$ are independent Wiener processes. While parameterizing stochastic forcings
 119 by the Wiener process appears to be reasonable, we note that the assumption of stochastic forcings as state-
 120 independent noise requires some justification. This is because real stochastic forcings may be functions of
 121 atmospheric states instead of having a constant variance. Because our focus here is on the relative roles
 122 of different stochastic parameterization methods in TC intensity rather than the physical nature of each
 123 forcing term, we will choose this constant-variance stochastic forcing as a protocol for the RF method to
 124 compare with the other random methods. More detailed discussion of this assumption can be found in
 125 (NKF, Fan et al., 2021b).

126 With the RF representation in terms of the Wiener process, the numerical solution of Eqs. (4)-(6) can be
 127 easily obtained by using Monte-Carlo simulations. Specifically in this study, the Runge-Kutta fourth order
 128 scheme is applied to the deterministic part of Eqs. (4)-(6) with a discretized time-step Δt , identical to that
 129 used in NKF. The stochastic part is then added to the model forcing at each time step, using a Gaussian
 130 random variable with variance $(\Delta t)\sigma_i^2$ for each state variable $i \in \{u, v, b\}$. Because of the constant variance
 131 for the stochastic forcings, this approach is essentially equivalent to the Euler-Maruyama first-order scheme.
 132 So long as the time step Δt is sufficiently small, this first-order accuracy suffices for representing the
 133 random processes as expected.

134 2.1.2 Random parameter (RP) representation

135 The second common method for parameterizing stochastic processes in numerical models is to randomize
 136 model parameters, based on a prior probability distribution of the parameters. A rationale behind this
 137 approach is that model parameters cannot be known accurately due to measurement uncertainties,
 138 incomplete understanding of physical processes, or the stochastic nature of phase transitions. For
 139 example, Zhang et al. (2015) implemented a mechanism that allows random fluctuation in the convective
 140 triggering function in an operational ensemble system, which is simply a numerical flag in the convection

141 parameterization of the Hurricane Weather Research and Forecasting (HWRF) model. Similarly, other
142 studies have applied the RP approach to, e.g., the boundary parameterization to reflect the unknown
143 variations in the land surface and/or boundary processes (Song et al., 2007; Plant and Craig, 2008; Doblas-
144 Reyes, 2009; Breil and Schädler, 2017). This RP scheme has been shown to improve the model overall
145 ensemble spread, thus capturing better the uncertainties of model physics than deterministic ensembles.

146 Given these inherent uncertainties of model parameters, we implement a scheme for the MSD model in
147 which three key model parameters including the tropospheric static stability (s), the sea surface temperature
148 T_s , and the surface drag coefficient (C_d) are randomized around a given mean value. Generally, such model
149 parameter randomization can be carried out in two different ways. In the first approach, random noise is
150 introduced to model parameters at the beginning of the model integration and kept unchanged during the
151 entire integration (hereinafter referred to as the *initial* RP approach). In the second approach, random noise
152 is added to model parameters every time step during the integration to reflect the variability of these model
153 parameters with time (hereinafter referred to as the *time-varying* RP approach).

154 While both the initial and time-varying RP approaches are practical and can be compared with each other,
155 their mathematical and physical interpretations are quite different and require detailed examinations. For
156 the initial RP approach, the uncertainties in the model parameters enter the system only as measurement
157 errors, which prevent one from determining the model parameters accurately. Thus, model parameters
158 take random values at the initial time but are fixed during the course of the model integration. In contrast,
159 the time-varying RP method accounts for the fact that model parameters are itself a random function of
160 time that must have a statistical distribution. An example for this is the convective triggering function in
161 cumulus parameterization, which determines if deep convective plumes can occur or not (Arakawa and
162 Schubert, 1974; Kain and Fritsch, 1990; Song et al., 2007; Suhas and Zhang, 2014; Zhang et al., 2015).
163 This triggering function often depends on vertical motion, CAPE, or some other ambient variables, and so
164 is inherently a random function of time. In this regard, the outcome from the initial RP and time-varying
165 RP representation could bring different insights into the variability of TC intensity that we wish to explore
166 herein.

167 To be specific for our implementation in this study, the three model parameters (s, T_s, C_d) are assumed
168 to be Gaussian random variables with known means and standard deviations. In nondimensional units,
169 the mean and standard deviation values are $\bar{s} = 0.1$ and $\sigma_s = 0.01$ for the static stability s , $\bar{T}_s = 1$ and
170 $\sigma_{T_s} = 0.1$ for SST T_s , and $\bar{C}_d = 1$ and $\sigma_{C_d} = 0.1$ for the surface drag coefficient C_d . These mean values
171 are based on their observed magnitude in real TC-force wind environment (see, e.g. Kieu, 2015; Zhang,
172 2010), while the standard deviations are assumed to be 10% of the mean values based on the typical
173 observational errors for TCs (see, e.g. Zhang, 2010; Richter et al., 2021). Because we wish to examine the
174 relative importance of RF and RP approaches, no random noise is added to the model forcings in both the
175 initial and time-varying RP implementations.

176 2.1.3 Random initial condition (RIC) representation

177 The last approach to take into account stochastic processes is to randomize model initial conditions, which
178 is by far the most common method to account for uncertainties in operational models (see, e.g. Hamill
179 et al., 2011; Aksoy et al., 2013; Aberson et al., 2015; Zhang and Weng, 2015; Tong et al., 2018). Often
180 known as ensemble forecasting, the RIC approach introduces noise with a given probability distribution
181 to model initial condition. This probability distribution comes from various pathways such as a prior
182 background covariance matrix (cold-start), ensemble cycling (breeding), or an analysis covariance matrix
183 (data assimilation), which are generally given at all model grid points.

184 Following the common practice of implementing random initial uncertainties in previous studies, our
185 RIC method adds white noise to the MSD model initial conditions, using a Gaussian distribution with a
186 given variance and zero mean. In the non-dimensional unit, the white noise for the RIC method with the
187 MSD model has a standard deviation of 0.01 for all (u, v, b) components. In full physical dimension, this
188 standard deviation respectively corresponds to $\sim 1m s^{-1}$ for wind and $\sim 0.5K$ for temperature, which are
189 reasonable for the random wind and temperature noise in real atmospheric conditions (Zhang, 2010; Zhang
190 et al., 2010). Note that unlike the RF or time-varying RP method for which the randomness is realized at
191 every time step, the RIC representation introduces random noise only at the initial time similar to the initial
192 RP method. Therefore, conditioned on the realization of the random initial condition, the MSD model is
193 deterministic at all time for the RIC method.

194 Given the above approaches to represent stochastic processes in the MSD model, Monte-Carlo simulations
195 of 1000 members are then carried out to examine the variability of TC intensity as well as the error growth
196 rate for each random representation method. In our range of Monte-Carlo experiments, we observe that an
197 ensemble of > 100 realizations are generally sufficient for a stable statistical distribution and significance.
198 Given the cheap computational cost of the MSD model, a fixed number of 1000 realizations is therefore
199 used for all the RIC, RP, and RF methods in this study such that the ensemble-size sensitivity analyses are
200 not necessary.

201 2.2 CM1 model experiments

202 While the MSD system could allow detailed examinations of the relative impacts of different random
203 representations due to its efficient computation and low order, real TCs are much more complex with
204 various nonlinear feedback between different dynamics and thermodynamics components that are not
205 accounted for in the MSD model. In addition, TC dynamics may contain chaotic behaviors at the MPI
206 equilibrium, which can mask out the stochastic effects that the MSD model could not capture (Kieu et al.,
207 2018; Keshavamurthy and Kieu, 2021, NKF).

208 To further evaluate the relative effects of random representations on TC intensity, the cloud model
209 (CM1, Bryan and Fritsch (2002)) is therefore employed in this study. By implementing different random
210 mechanisms in the CM1 model, one can verify what results obtained from the MSD system are valid in a
211 more complete full-physics model and thus applicable to real TCs. For our herein study, the axisymmetric
212 setting of the CM1 model was used such that the results from CM1 model can be used to verify those
213 obtained from the MSD model under the same axisymmetric framework. Comparing analyses from the
214 low-order MSD model and the full-physics CM1 model can therefore provide more understanding into the
215 impacts of random noise on the variability and the error growth of TC intensity.

216 Because of the large computational requirement and the numerical stability of the CM1 model, it is
217 noted that our implementation of the RF method for the CM1 model is slightly different from that for the
218 MSD model. Specifically, we apply additive white noise to the momentum and temperature equations
219 with a constant standard deviation of $[0.1 - 0.5]m s^{-1}min^{-1}$ for wind and $[10^{-3} - 10^{-2}]K min^{-1}$ for
220 temperature, respectively (Zhang, 2010; Zhang et al., 2010). The constant variance design is to ensure the
221 closest possible resemble to the RF implementation for the MSD system described in the previous section.
222 It also helps maintain the same order of the finite difference accuracy for the deterministic part, which is
223 based on the Runge-Kutta scheme in the CM1 model. No random noise is, however, added to the model
224 moisture state variable due to unknown probability distributions of moist variables/graupel species. Our
225 attempt to add random noise to moist variables did not show any significant difference in terms of model
226 intensity output, yet the noise decreases the stability of the CM1 model and prevents us from examining a

227 range of noise amplitude dependence. Thus, no random perturbations are applied to the moist equations in
228 all of our CM1 experiments herein.

229 Regarding the RIC method, our approach for the CM1 model is identical to that for the MSD model. That
230 is, white noise with a range of standard deviations from 0.01 to 0.1 $m s^{-1}$ is added to the CM1 model initial
231 conditions. Likewise, the implementation of the RP method for the CM1 model is also identical to that
232 used in the MSD model. It should be noted, nonetheless, that CM1 has a large number of model parameters
233 that can be randomized. For the sake of comparison with the MSD model, two specific parameters that
234 are directly relevant to TC intensity in CM1 including the sea surface temperature (T_s) and the surface
235 drag (C_d) are chosen in our RP experiments with the CM1 model. These parameters are assumed to be
236 random variables with standard derivation of 1° K for T_s and 10^{-4} for C_d , respectively. The mean values
237 for these parameters are then varied in the range of [298 – 305°K] for T_s and [10^{-3} – 3×10^{-3}] for C_d
238 such that the dependence of TC intensity variability on different mean values of model parameters can be
239 also studied. Note that tropospheric stratification is a parameter in the MSD model, but it is a diagnostic
240 variable in CM1. Therefore, its random parameterization cannot be implemented in the CM1 model.

241 Due to the computational limit and a large number of model output, a fixed number of 100 realizations
242 are conducted for each random noise amplitude in the CM1 experiments, regardless of the random
243 representation method. Our ad-hoc sensitivity analyses for ensemble members ranging from 100-200 show
244 again insignificant difference in terms of statistics when the number of realizations changes. Thus, no
245 ensemble size sensitivity experiment for CM1 will be provided.

246 2.3 An error growth algorithm

247 To evaluate the effects of random noise on TC intensity error growth, we follow the approach in Kieu
248 et al. (2018) and introduce small noise along a reference state at different stages of TC development. This
249 type of a state-dependent error growth rate is to mimic the real-time forecast cycles by which TC intensity
250 forecasts are re-initialized every 6 or 12 hours. As TCs evolve, their intensity changes and TC intensity
251 errors may therefore evolve differently, even with the same initial error. Examining how such an *intensity*
252 *error growth rate* changes with time will allow forecasters to estimate how the accuracy of their intensity
253 forecast varies during TC development.

254 In quantifying the dependence of intensity error growth on the stage of TC development, it is important
255 to note that all environmental conditions must be fixed so that such dependence can be well-defined. This
256 is because any change in environmental conditions would cause not only changes in TC intensity along the
257 trajectory but also a shift in the MPI equilibrium, which produces an unexpected intensity error variability.
258 This is a subtle point in studying TC intensity errors, yet it has not been sufficiently emphasized in previous
259 studies that we wish to emphasize again here.

260 With this approach, our algorithm for computing TC intensity error growth in the MSD model includes
261 the following steps

- 262 1. Select any initial state $x_0 = (u_0, v_0, b_0)$, where $v_0 > 0$ and generate a reference orbit $x_f(t) =$
263 $(u_f(t), v_f(t), b_f(t))$ during a given interval $t \in [0, T]$, based on the deterministic MSD system (1)-(3)
264 (see the thick black line in Figure 1(a));
- 265 2. Choose a given time τ and its corresponding reference state $x_f(\tau)$ at the time τ to add a random
266 perturbation vector ξ to x_τ , where $\xi = (\xi_u, \xi_v, \xi_b)$ are independent Gaussian variables with zero mean
267 and standard deviations $\{\sigma_u, \sigma_v, \sigma_b\}$ respectively. This process gives us an initially perturbed state
268 $x_f(\tau) + \xi$ at time τ (see the crosses in Figure 1a);

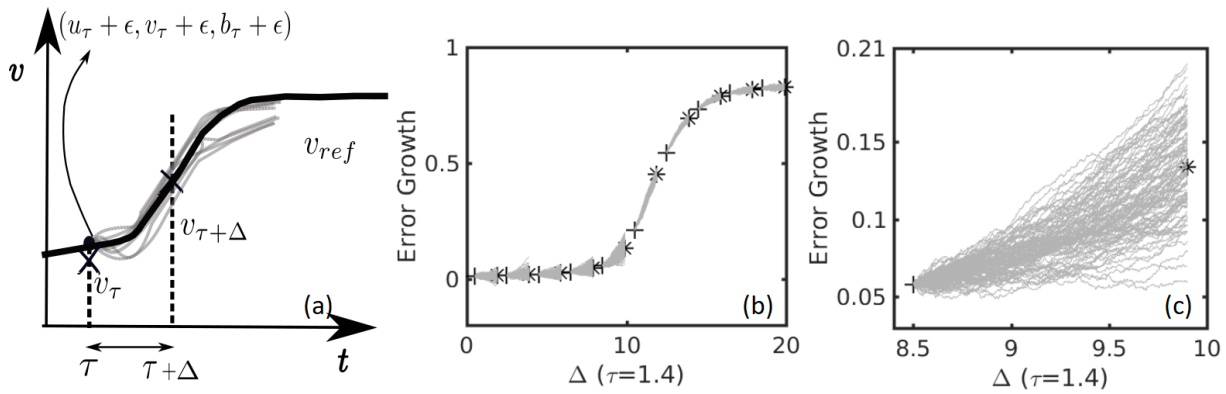


Figure 1. A schematic diagram illustrating the algorithm for calculating TC intensity error growth at different stages of TC development for (a) a reference orbit (solid black) and an ensemble of perturbed stages at the beginning time τ and the end of the perturbation integration $\tau + \Delta$ (crosses); (b) time series for a range of stages starting from τ and ending at $\tau + \Delta$ for $N = 1000$ realization; and (c) a magnified version of (b) for one specific stage. Note that pluses and asterisks in (b)-(c) show the points on the deterministic orbit at time τ when perturbations are added and at time $\tau + \Delta$ where the error growth rate is computed, respectively.

- 269 3. Denote the components of the perturbed state at τ as $(u'(\tau), v'(\tau), b'(\tau)) \equiv x_f(\tau) + \xi$, we then choose
 270 a lead time Δ and integrate $(u'(\tau), v'(\tau), b'(\tau))$ from 0 to Δ , using the same MSD model as for the
 271 reference integration;
- 272 4. For each pair (τ, Δ) , repeat steps 2-3 a number of times, say $N = 1000$ times, to generate an ensemble
 273 of integration from the initially-perturbed state $(u'(\tau), v'(\tau), b'(\tau))$. Note that different realizations
 274 of the Gaussian distribution will give different ξ , even with the same values of mean and standard
 275 deviation. Store all of these integrated states and denote their corresponding states at $t = \tau + \Delta$ as
 276 $(u_i(\tau + \Delta), v_i(\tau + \Delta), b_i(\tau + \Delta)), i = 1..N$ (see the triangles in Figure 1b));
- 277 5. Compute the root mean square error $err(\tau, \Delta)$ for the $v_i(\tau + \Delta)$ component with respect to the
 278 reference component $v_f(\tau + \Delta)$ for each time τ and lead time Δ as follows

$$err(\tau, \Delta) = \sqrt{\frac{1}{N} \sum_{i=1}^N \left(\frac{v_i(\tau + \Delta) - v_f(\tau + \Delta)}{\Delta} \right)^2}, \quad (7)$$

279 which is defined hereinafter as *the intensity error growth rate* corresponding to the lead time Δ at the
 280 forecast cycle τ .

- 281 6. Repeat steps 1-5 for different values of τ and Δ to obtain the distribution of the error growth rate as a
 282 function of (τ, Δ) .

283 By varying τ , the error growth calculation as outlined above can capture the characteristics of TC
 284 intensity error at different stages of TC development. Likewise, varying Δ will allow us to examine how
 285 TC intensity error growth changes with forecast lead times similar to what carried out in real-time intensity
 286 verification. Note that our definition of the intensity error growth in Eq. (7) is relative to a given reference
 287 state $v_f(\tau + \Delta)$. If one replaces this reference state by the corresponding ensemble mean, Eq. (7) would
 288 give us an ensemble spread instead of the absolute intensity errors. Since our focus here is on the growth of
 289 the absolute error rather than ensemble mean, definition (7) is therefore adopted here.

Table 1. Configuration of Monte-Carlo simulations for the stochastic MSD model (4)-(6). Details of physical interpretations and scaling analyses of these parameters can be found in KW17.

Parameter	Value	Remark
Δt	0.01	nondimensional time step
T	50	nondimensional duration of the Monte-Carlo simulation
p	200	nondimensional square ratio of the PBL depth over the radius of the maximum wind
r	0.1	a nondimensional parameter representing the radiative cooling
s	0.1	a nondimensional parameter representing the tropospheric stratification
C_d	1	a nondimensional parameter representing the surface drag coefficient
T_s	1	a nondimensional parameter representing the surface temperature
σ_u	0.01	nondimensional variance of the u -wind stochastic forcing component
σ_v	0.01	nondimensional variance of the v -wind stochastic forcing component
σ_b	0.01	nondimensional variance of the buoyancy stochastic forcing component

290 Although the same steps are carried out for all three random representation methods, we should mention
 291 that different realizations of ξ are added to the initial state only for the RIC method, because the MSD
 292 system (1)-(3) is deterministic. For the RF method, stochastic forcing varies every time step and so there
 293 is no need to randomize the initial state. For the RP method, whether one applies different realizations
 294 of the initial perturbation ξ would depend on what RP scheme, i.e., the initial or time-varying, is used as
 295 discussed in the previous section.

3 FIDELITY-REDUCED MODEL RESULTS

296 In this section, we present first the analyses of different random representation methods for TC intensity in
 297 the MSD model, using two key measures including i) TC intensity variability at the maximum equilibrium,
 298 and ii) intensity error growth. The first measure provides insights into TC intensity error saturation at
 299 long forecast lead times, which plays a key role in estimating TC intensity predictability as discussed
 300 in Kieu and Moon (2016); Kieu et al. (2018). The second measure focuses on how the characteristics
 301 of TC intensity error growth change during TC development, which are of relevance to the reliability of
 302 operational forecast. These two aspects of TC intensity can be thoroughly examined within the low-order
 303 MSD model and compose the main results of this section.

304 3.1 Intensity variability at the mature stage

305 To have a broad picture of TC intensity in our stochastic MSD model, Figure 2 shows the time series of
 306 the v -component in the MSD system as obtained from the Monte-Carlo simulations with the RF method.
 307 These simulations have the same numerical procedure and settings as in NKF, which are summarized
 308 in Table 1. Note that the v component represents the maximum tangential wind near the surface in the
 309 TC-scale dynamics. Thus, it can be used as a proxy to examine TC intensity as well as related variability in
 310 all of hereinafter analyses.

311 As shown in Figure 2, the Monte-Carlo simulations of Eqs.(4)-(6) overall capture expected TC
 312 development, with three distinct phases in all realizations including a pre-condition (genesis) period,
 313 rapid intensification, and finally the maximum intensity equilibrium stage. While the exact onset moment
 314 of rapid intensification highly varies among realizations (Fan et al. (2021b)), these three stages are well
 315 displayed and reflect the inherent TC development in the MSD model under idealized environment, even in
 316 the presence of random noise. Despite similar intensification rate among all realizations, the stochastic
 317 nature in the MSD model is manifested in Figure 2 as non-smooth fluctuations of TC intensity every time

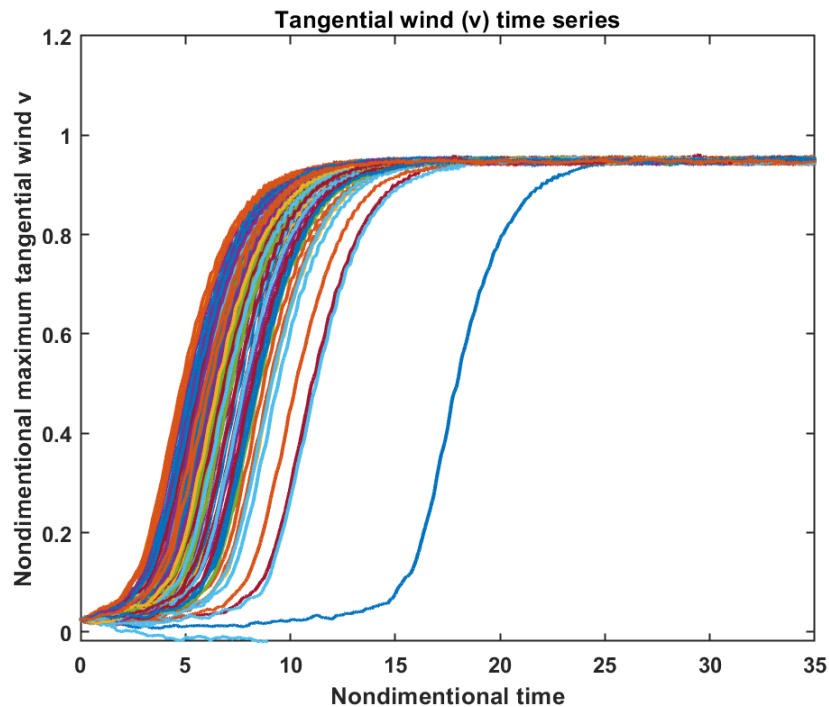


Figure 2. Time series of the tangential wind component v as obtained from 1000 Monte-Carlo simulations of the MSD system, using the random forcing representation with noise amplitude $\sigma = 0.01$. Model initial condition is set as $(-0.01, 0.01, 0.01)$, and other model parameters are $p = 200, s = 0.1, r = 0.25, C_d = 1.0, T_s = 1.0$.

318 step along any trajectory. So long that the model parameters are fixed, the random forcing thus affects only
 319 fluctuations around the main trajectory but not the averaged state of TC development. As the RF amplitude
 320 increases, TC mean state is no longer maintained and intensification rate or MPI will be different. In this
 321 regard, these Monte-Carlo simulations confirm not only the main characteristics of TC development but
 322 also the stochastic property of the MSD system (4)-(6) with the RF representation as expected.

323 Of more interest for our analyses is however the variability of TC intensity at the maximum intensity
 324 equilibrium due to stochastic forcing, which dictates the limit in our ability to reduce TC intensity forecast
 325 errors. To examine how this variability depends on the amplitude of each RF in Eqs. (4)-(6), Figure 3 shows
 326 the standard deviation of v (denoted hereinafter as Γ) as a function of $(\sigma_u, \sigma_v, \sigma_b)$ during the equilibrium
 327 stage (i.e., $t = 25 - 50$ in Figure 2). Consistent with results in (Nguyen et al., 2020, Figure 4 therein),
 328 TC intensity fluctuations increase almost linearly with σ_u and σ_v , so long as these RF amplitudes are
 329 sufficiently small (≤ 0.05 in nondimensional unit). Such an asymptotically linear increase of Γ for the small
 330 noise can be proven rigorously, based on the stationary distribution as shown in NKF.

331 For the stochastic forcing component σ_b , we note that Γ differs somewhat from a linear function, because
 332 it is possible that TC intensity deviates far away from the equilibrium when σ_b is sufficiently large and the
 333 underlying stability assumption for the MSD system is thus no longer valid. Consistent with the finding in
 334 NKF, we notice also that the stochastic forcing for tangential wind or warm core anomaly has the most
 335 impacts on overall TC intensity variability (Figure 3b-c), which produces intensity fluctuation one order of
 336 magnitude larger than that caused by the radial wind stochastic forcing (Figure 3a).

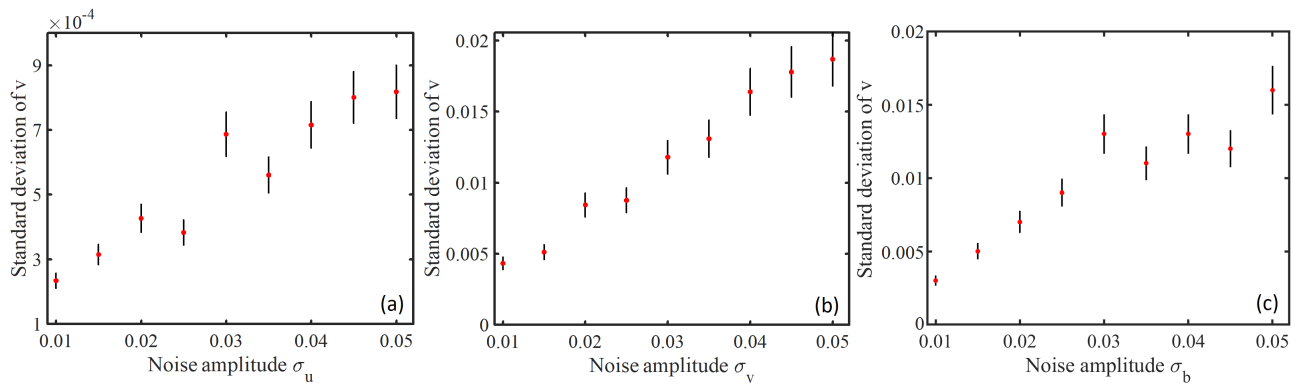


Figure 3. The standard deviation of the v component for the RF representation method as a function of the stochastic forcing standard deviation added to (a) the u forcing, (b) the v forcing, (c) and the b forcing in the MSD system.

337 Relative to the RF method, Figure 4 shows a similar dependence of Γ on each model parameter at the
 338 MPI equilibrium obtained from the initial and time-varying RP methods. Overall, intensity fluctuation
 339 increases with the magnitude of the parameter variance for both the RP implementations, similar to that
 340 with the RF method. One notices however a fundamental difference between the RP and RF methods in
 341 terms of the magnitude of Γ . Specifically for the initial RP method (Figure 4a-c), Γ is of the same order of
 342 magnitude as in the RF method. In contrast, the time-varying RP method (Figure 4e-f) captures almost one
 343 order of magnitude smaller regardless of model parameters. This is an noteworthy point, since it suggests
 344 that the randomness of the model parameters during TC development plays a less important role in TC
 345 intensity variability than the initial uncertainty in these model parameters. From a practical standpoint, this
 346 non-trivial result implies that our efforts in improving model parameters at the initial time will have more
 347 effects on TC intensity variability as compared to randomly sampling model parameters during the course
 348 of model integration.

349 From the mathematical standpoint, such different behaviors of intensity variation between the initial and
 350 the time-varying RP approaches can be understood if one analyzes the intensity probability distribution at
 351 the equilibrium as in NKF. Indeed, sensitivity analyses of the intensity variance for the initial RP method at
 352 the MPI limit (Appendix 1) show that the tropospheric static stability parameter s plays a smaller role in
 353 the overall variability of TC intensity when s is small. As s becomes sufficiently large (>0.04), the MSD
 354 system becomes bifurcated Kieu and Wang (2018) and the deviation around the MPI equilibrium becomes
 355 much larger, thus resulting in larger Γ as seen in Figure 4c. On the contrary, the SST and surface drag
 356 coefficient parameters do not possess any bifurcation point. Therefore, Γ increases almost linearly with
 357 the random noise amplitude for the initial RP representation¹. This result highlights the critical role of
 358 the tropospheric static stability in determining TC intensity variability as compared to C_d or SST (KW17,
 359 Kieu et al., 2021).

360 Unlike the initial RP method for which the MPI may settle down to different equilibria for different
 361 parameters, the time-varying RP method has a much more intriguing behavior. Here we study an important
 362 property of a linear stochastic system with time-varying random parameters for which the fluctuation of
 363 the system around its stable point approaches zero as the numerical time step becomes finer (See Appendix

¹ Technically, this property is related to the fact that the MSD model can be treated as an extended Markov system (u, v, b, s, T_s, C_d) . For this extended system, one first obtains the stationary distribution μ by solving the equation $\mathcal{L}^* \mu = 0$ for the stationary distribution μ , where \mathcal{L}^* is the adjoint of the generator \mathcal{L} of the Markovian system. Then, the error growth at a large time limit can be approximated by the standard deviation of the v -component under the stationary distribution.

364 2). This counter-intuitive behavior in the presence of pure random parameters is because a finer time step
 365 prevents the model state from deviating too far from its equilibrium at each iteration, leading to an overall
 366 smaller fluctuation with time when the time step decreases. While the MSD system is far from being
 367 linear, the MSD system under random forcing does capture smaller Γ for a smaller time step in our series
 368 of experiments, much like a linear system (not shown). This particular property of the time-varying RP
 369 indicates the subtle dependence of TC intensity variability on the way one implements the RP representation
 in TC models as shown in Figure 4.

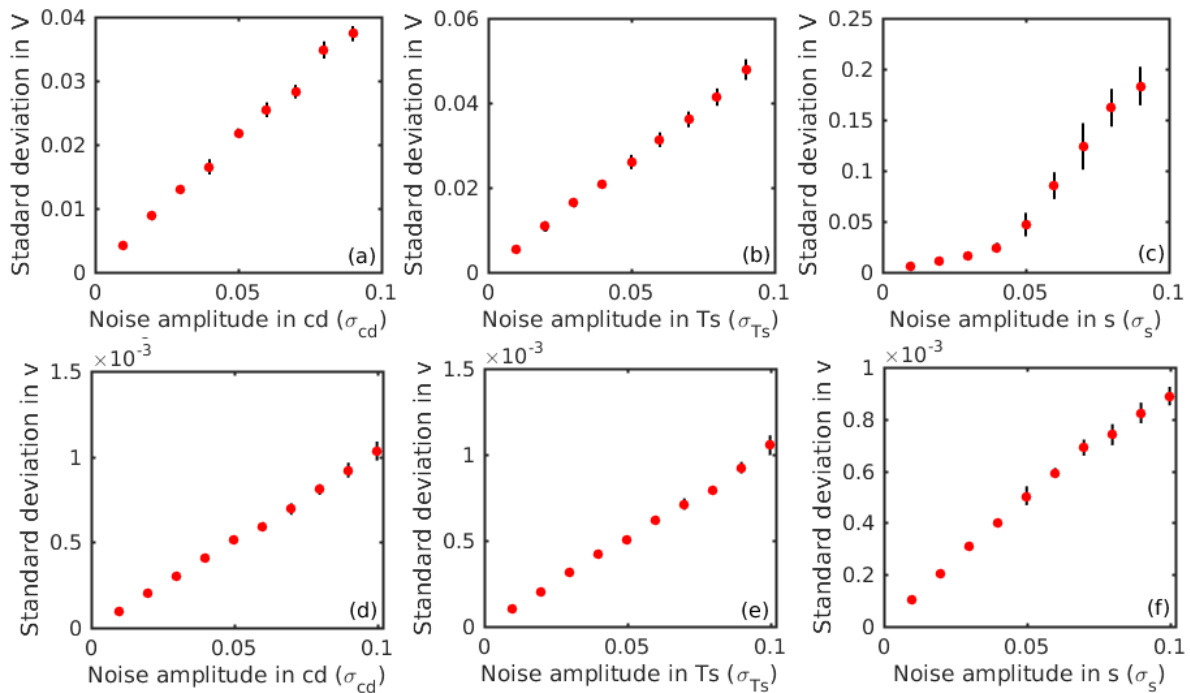


Figure 4. Similar to Figure 3 but for the RP representation as a function of the random standard deviation for (a)-(c) initial RP and (d)-(f) time-varying RP method.

370

371 Although the initial and time-varying RP methods result in different response of TC intensity to random
 372 parameters, it is of interest to note that Γ is somewhat the same among the three model parameters for
 373 each method in terms of the magnitude. This indicates that the random fluctuation of each parameter could
 374 equally induce TC intensity variability that one has to take into account. Of course, these relative roles
 375 among these parameters as shown in Figure 4 are very specific to the MSD model. Therefore, it is necessary
 376 to further verify these properties in full physics models as will be shown in Section 4.

377 Unlike the RF or RP approach for which the stochasticity can take place at every time step, the RIC
 378 method is different due to the deterministic nature of the underlying model. We note again that the MSD
 379 model contains a single stable point that corresponds to the MPI equilibrium as shown in KW17. As
 380 such, regardless of initial conditions, all trajectories will eventually converge to a single MPI point after
 381 sufficiently long time. In the absence of stochastic forcing or random parameters, the intensity variability at
 382 the MPI equilibrium in the MSD model must therefore approach zero irrespective of the initial random
 383 components as confirmed in Figure 5. Apparently, this deterministic characteristic of the MSD system
 384 prevents it from modelling TC intensity variability at the MPI limit, unless stochastic forcing or random
 385 parameters are used.

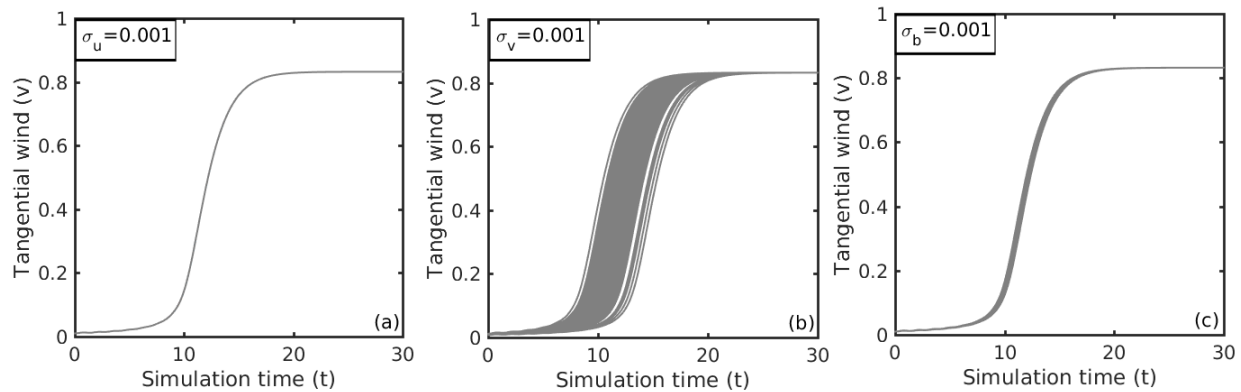


Figure 5. Time series of tangential wind v for a fixed noise amplitude $\sigma_{u,v,b} = 0.001$ that is added to initial condition (a) u_0 , (b) v_0 , (c) b_0 respectively, where the initial condition $(u_0, v_0, b_0) = (-0.01, 0.01, 0.01)$, and other model parameters are $p = 200$, $s = 0.1$, $r = 0.25$, $C_d = 1.0$, $T_s = 1.0$

386 We wish to mention at this point that real TC dynamics is far more complex than a single stable point at
 387 the equilibrium captured by the MSD system as shown in Figure 5. As discussed in previous studies (e.g.
 388 Hakim, 2011; Brown and Hakim, 2013; Kieu and Moon, 2016), long simulations of any full-physics TC
 389 model always display a quasi-stationary equilibrium instead of a stable fixed point as in the MSD system
 390 or the theoretical MPI framework. Such intensity fluctuation at the MPI limit in real TC models could be
 391 attributed to several factors such as process noises, truncation errors, or the existence of low-dimensional
 392 chaotic dynamics; none of which is captured by the MSD system. To better compare the relative effects of
 393 the RIC, RF and RP methods in representing random effects on TC intensity, one must ultimately employ
 394 full physics models. For the MSD system, we could at least conclude that the RF method produces the
 395 largest impacts on TC intensity variability at the long lead times, followed by the initial RP method. To
 396 what extent this can be realized in full-physics CM1 models will be presented in Section 4.

397 3.2 Error growth during RI

398 Along with the variability of TC intensity at the equilibrium, it is necessary to examine also how intensity
 399 fluctuation varies during TC development. In this regard, Figure 6 shows the TC intensity error growth
 400 rate $err(\tau, \Delta)$ as a function of forecast lead time τ for the RF method. Recall that the error growth rate is
 401 computed along a reference trajectory with a prescribed lead time Δ . Thus, $err(\tau, \Delta)$ depends on both the
 402 integration time (τ) and the lead time Δ as discussed in Section 2.3.

403 Regardless of the forecast lead time Δ , one can see in Figure 6 a very specific pattern of $err(\tau, \Delta)$,
 404 with the most rapid growth during the pre-conditioning stage, followed by a quick decrease during the
 405 intensification period and eventually approaching a constant growth rate at the MPI equilibrium. That
 406 $err(\tau, \Delta)$ is maximum prior to rapid intensification reflects the fact that the onset moment of TC rapid
 407 intensification highly varies among different realizations in the MSD system (cf. Figure 2. See also Fan
 408 et al. (2021b) for a rigorous treatment), thus resulting in large intensity errors. As the vortex enters its
 409 intensification period, TC dynamics becomes more consistent among all realizations, which explains the
 410 decrease in the error growth. In contrast, the growth rate is minimum when the TC vortex reaches its
 411 equilibrium stage, because this equilibrium is highly stable and resilient to random fluctuation (Kieu, 2015,
 412 NKF). As a result, $err(\tau, \Delta)$ subsides and levels off for $\tau > 16$. These behaviors of the intensity error
 413 growth rate accord with previous study using a full-physics model Kieu et al. (2018) and highlight the
 414 unique properties of TC intensity errors.

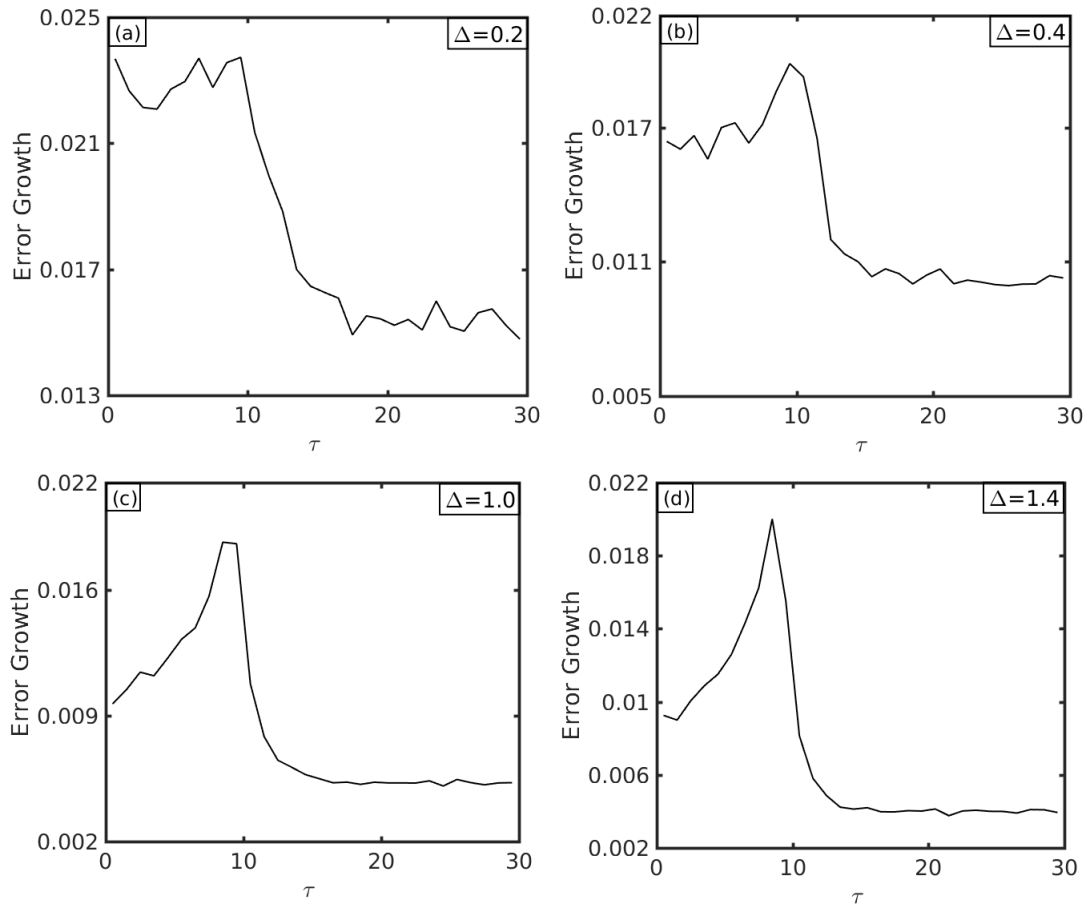


Figure 6. The intensity error growth rate $err(\tau, \Delta)$ for different values of the forecast lead time Δ and the stage of development (τ) as obtained from the RF method, using the same set of model parameters as in Figure 3 with $\sigma_u = \sigma_v = \sigma_b = 0.01$. Here, a fixed perturbation amplitude $\epsilon = 0.001$ and $N = 1000$ realizations are used for all error growth integration.

415 Of further significance is that the overall error growth characteristics of $err(\tau, \Delta)$ appear to less
 416 sensitive to the forecast lead time Δ , so long as Δ is not too large. Note however for the RF method that
 417 $err(\tau, \Delta)$ is smaller for a longer lead time Δ as shown in Figure 6. This smaller error growth rate for
 418 a longer lead time is because TC intensity is bounded by the maximum equilibrium. Therefore, a long
 419 forecast lead time Δ must eventually result in a reduced error growth rate as seen from Eq. (7) as TC
 420 intensity approaches the MPI limit Kieu et al. (2018), consistent with what shown in Figure 6.

421 For the RIC method, a very similar behavior of $err(\tau, \Delta)$ is captured, with the maximum rate during the
 422 pre-conditioning period, followed by a decrease during rapid intensification and a stable value at the MPI
 423 limit (Fig. 7). This similar behavior between the RIC and RF representations suggests that different error
 424 growth rates at different stages of TC development are inherent to TC dynamics, regardless of the presence
 425 of random noise in the initial condition or forcing.

426 Regarding the RP method, one notices somewhat different behaviors of $err(\tau, \Delta)$ as compared to the
 427 RIC or RF methods, depending on which model parameters are used and whether the RP method employs
 428 the initial or time-varying implementation (Figure 8). For the initial RP approach, the overall properties of
 429 $err(\tau, \Delta)$ for the static stability parameter s are almost the same as those with the RF or RIC method. That
 430 is, the maximum error growth rate occurs during the pre-conditioning period, followed by a decreasing

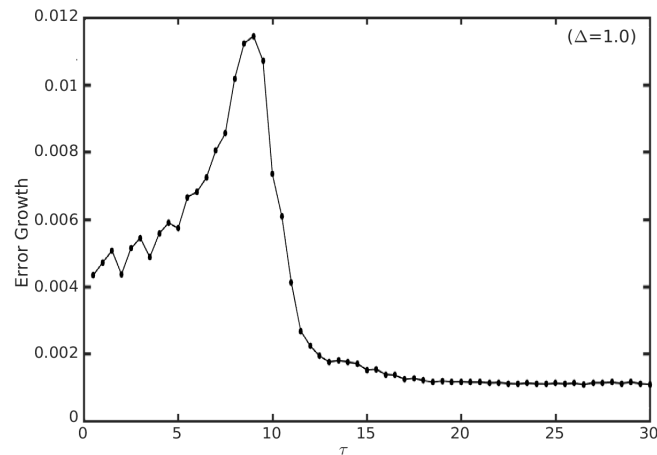


Figure 7. Similar to Figure 6 but for the RIC method, assuming the same set of model parameters as in Figure 6 and a fixed lead time $\Delta = 1.0$.

431 period and level off at the MPI equilibrium (Figure 8a). In contrast, both SST and surface drag parameters
 432 show a quick increase in the error growth rate at first, but then maintain a large error growth rate during the
 433 entire subsequent stage of TC development, instead of subsiding over time as for the RF or RIC method.
 434 This unique behavior of $err(\tau, \Delta)$ for T_s and C_d is due to the fact that the uncertainty magnitude of these
 435 parameters is much larger than that of s at the equilibrium, even though the relative percentage is the same.
 436 One can see this directly by looking at the sensitivity analyses for the initial RP method (see Appendix
 437 1). Apparently, the same 10% variability of each parameter would give a different absolute magnitude
 438 in the RP method. That is, a 10% variability of s would give an absolute uncertainty magnitude of 0.01,
 439 whereas the same 10% variability of T_s or C_d would result in an absolute uncertainty magnitude of 0.1.
 440 This explains the difference in the error growth rate at the mature stage as seen in Figure 8 for the initial
 441 RP implementation.

442 For the time-varying RP implementation, $err(\tau, \Delta)$ is about one order of magnitude smaller than what
 443 obtained from the initial RP method. Recall that such a large difference of $err(\tau, \Delta)$ between the initial
 444 and time-varying RP approaches is not unique to the rapid intensification period, but it is in fact true for the
 445 MPI equilibrium as well (cf. Figure 4). This is noteworthy, because it suggests that both the RF and the
 446 initial RP methods produce more intensity errors than randomizing model parameters during the course
 447 of TC development. Again, this conclusion should be cautioned, because it is drawn from a simple MSD
 448 system that may or may not fully reflect real TC development. Further verification of these results in the
 449 full-physics CM1 model will be presented in the next section, for which we now turn to.

4 CM1 MODEL RESULTS

450 Although the results obtained from the low-order MSD system are significant, various simplifications in
 451 the MSD model naturally raise a question of how much these results can be realized in real TCs. In this
 452 section, we examine similar properties of TC intensity error growth and saturation for the CM1 model,
 453 using the same random representation methods as for the MSD system. Unlike the MSD model, it should be
 454 emphasized that the CM1 model does not converge to a single MPI equilibrium (Figure 9a), even with the
 455 axisymmetric setting. Instead, CM1 reaches a statistical quasi-equilibrium state due to possible existence
 456 of low-dimensional chaos at the MPI limit that the MSD model cannot capture as mentioned in Section

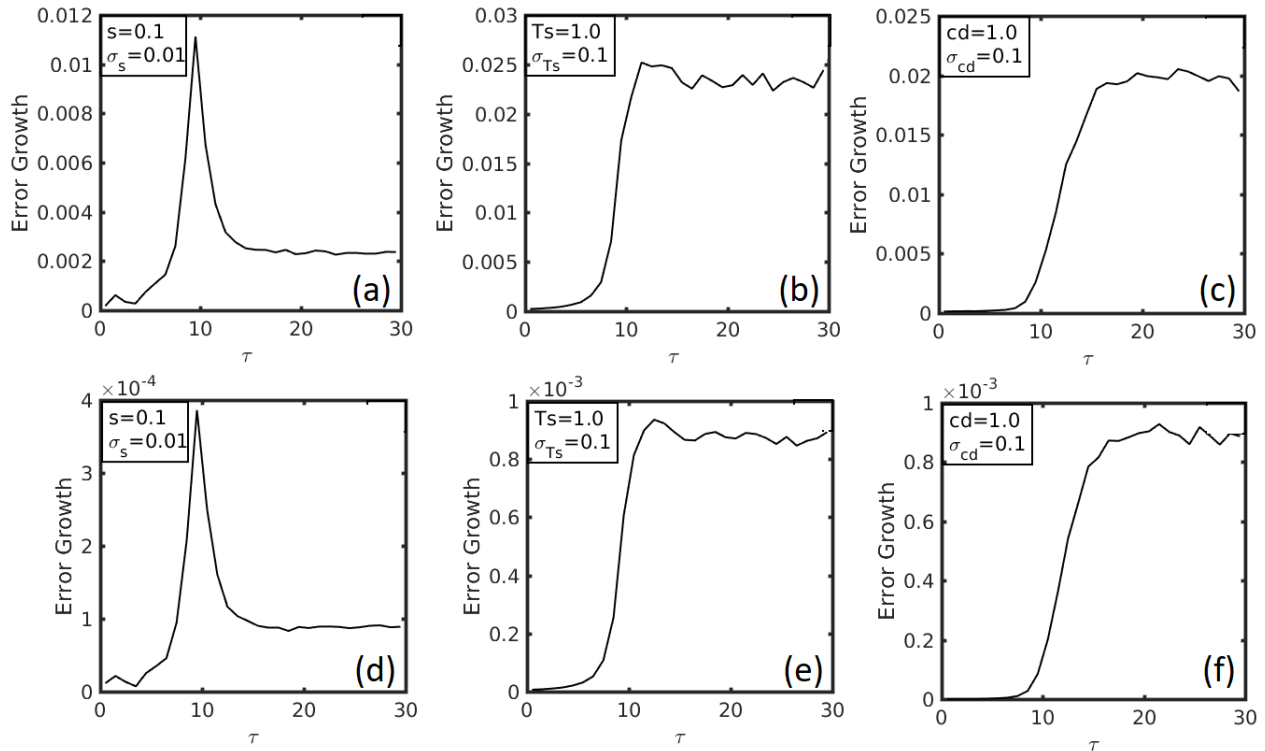


Figure 8. Similar to Figure 6 but for the random parameter approach with (a)-(c) initial RP method, and (d)-(f) time-varying RP method.

457 2.2 Kieu and Moon (2016); Kieu et al. (2018). Thus, the MPI equilibrium must be now understood in a
 458 statistical sense for all analyses in this section.

459 **4.1 Intensity variability at the MPI equilibrium**

460 Figure 9b shows the standard deviation of TC intensity fluctuation (hereinafter denoted as Γ_{MMI} to
 461 distinguish from Γ obtained from the MSD system) as a function of noise amplitudes in the RF simulation,
 462 which is averaged during the CM1 quasi-stationary maximum intensity (MMI^2) stage. With more realistic
 463 physics, one notices in Figure 9b that the intensity variability tends to increase with the amplitude of
 464 stochastic forcing, similar to what obtained from the MSD model. This result may look at first somewhat
 465 trivial but it is in fact very noteworthy. Indeed, such an increase of Γ_{MMI} indicates that stochastic forcing
 466 can actually introduce further variability to TC intensity, even in the presence of possible low-dimensional
 467 chaos at the MMI equilibrium. As discussed in, e.g., (Sugihara et al., 1994, NKF), stochastic and chaotic
 468 variability are generally different, because deterministic chaos can exist without any stochastic forcing. The
 469 fact that Γ_{MMI} increases with random noise amplitude seen in Figure 9b suggests that stochastic forcing
 470 could contribute to intensity errors at long lead times beyond the chaotic dynamics, if the stochastic forcing
 471 is sufficiently large.

472 For the RP method, different intensity variability between T_s and C_d is captured (Figure 10). For T_s , both
 473 MMI and Γ_{MMI} increase with SST, consistent with previous studies (Keshavamurthy and Kieu, 2021).
 474 While the increase of MMI with T_s is well understood, the increase of Γ_{MMI} with T_s is of note here, as it

² It should be noted that the actual CM1 model maximum intensity (MMI) is generally different from the theoretical MPI value.

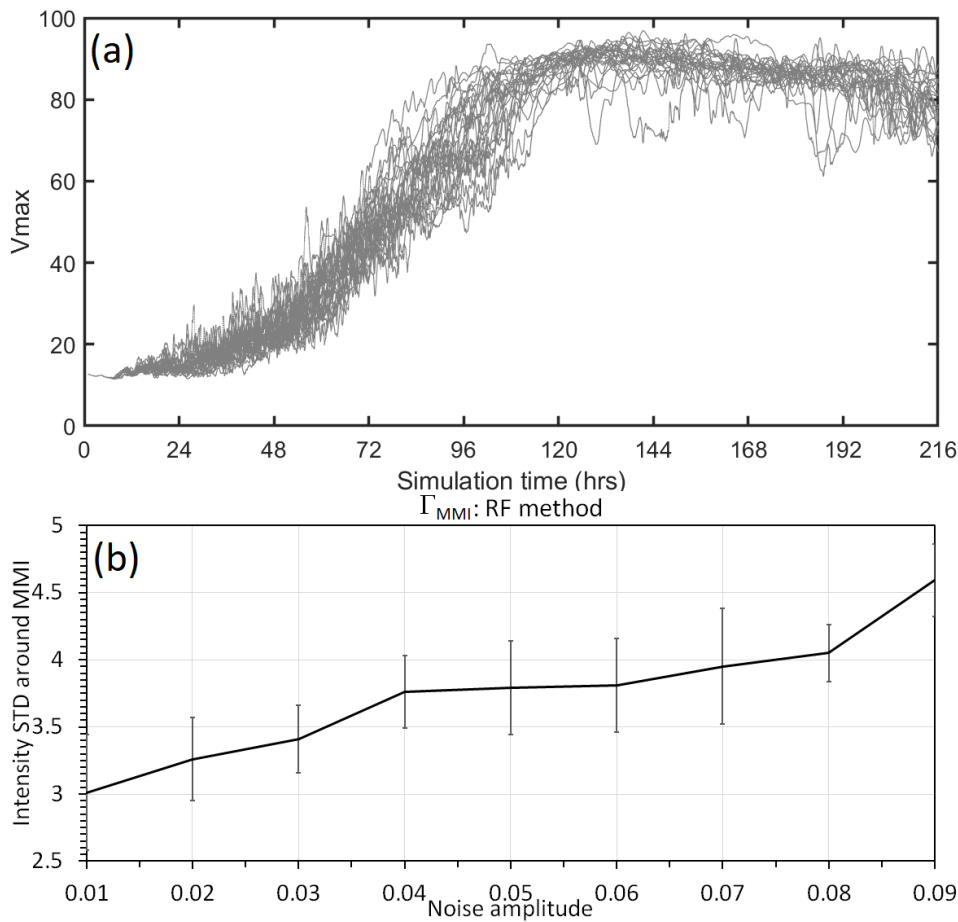


Figure 9. a) Time series of the maximum tangential wind (V_{MAX} , unit ms^{-1}) as obtained from 100 20-day simulations of the CM1 model that is implemented with the RF method; and (b) the standard deviation of V_{MAX} (unit, ms^{-1} at the maximum intensity equilibrium (day 9-18 into integration) as a function of the random forcing standard deviation. Error bars denote 95% confidence intervals.

475 indicates that a warmer SST would also result in higher uncertainty for intensity forecast (Kieu and Moon,
 476 2016; Keshavamurthy and Kieu, 2021).

477 In contrast, the surface drag coefficient shows a decrease of MMI for a larger C_d as generally expected, yet
 478 Γ_{MMI} first decreases and then increases with C_d (Figure 10d). This unique behavior of intensity variability
 479 in the C_d experiment is due to the dual role of C_d in determining both the MMI and the uncertainty. That
 480 is, when C_d increases from a small value, it will reduce both MMI and the fluctuation around the MMI due
 481 to the nature of the frictional forcing against motion. When C_d is sufficiently large, MMI is however too
 482 weak that it is no longer able to “trap” the intensity fluctuation, and so the fluctuation of intensity around
 483 the MMI equilibrium becomes larger as discussed in NKF.

484 Given such dependence of MMI and the variability around MMI on T_s and C_d in the RP method,
 485 Figures 11b-c show how Γ_{MMI} depends on the random noise amplitude of T_s and C_d in the CM1 model.
 486 Here, we present results only for the initial RP approach because the time-varying RP method produces a
 487 much smaller intensity variability as compared to the initial RP method in the CM1 model.

488 Unlike the MSD model, Γ_{MMI} does not seem to increase with the noise amplitude for the initial RP
 489 method. The same is also true for the RIC method when increasing the random noise amplitude of initial

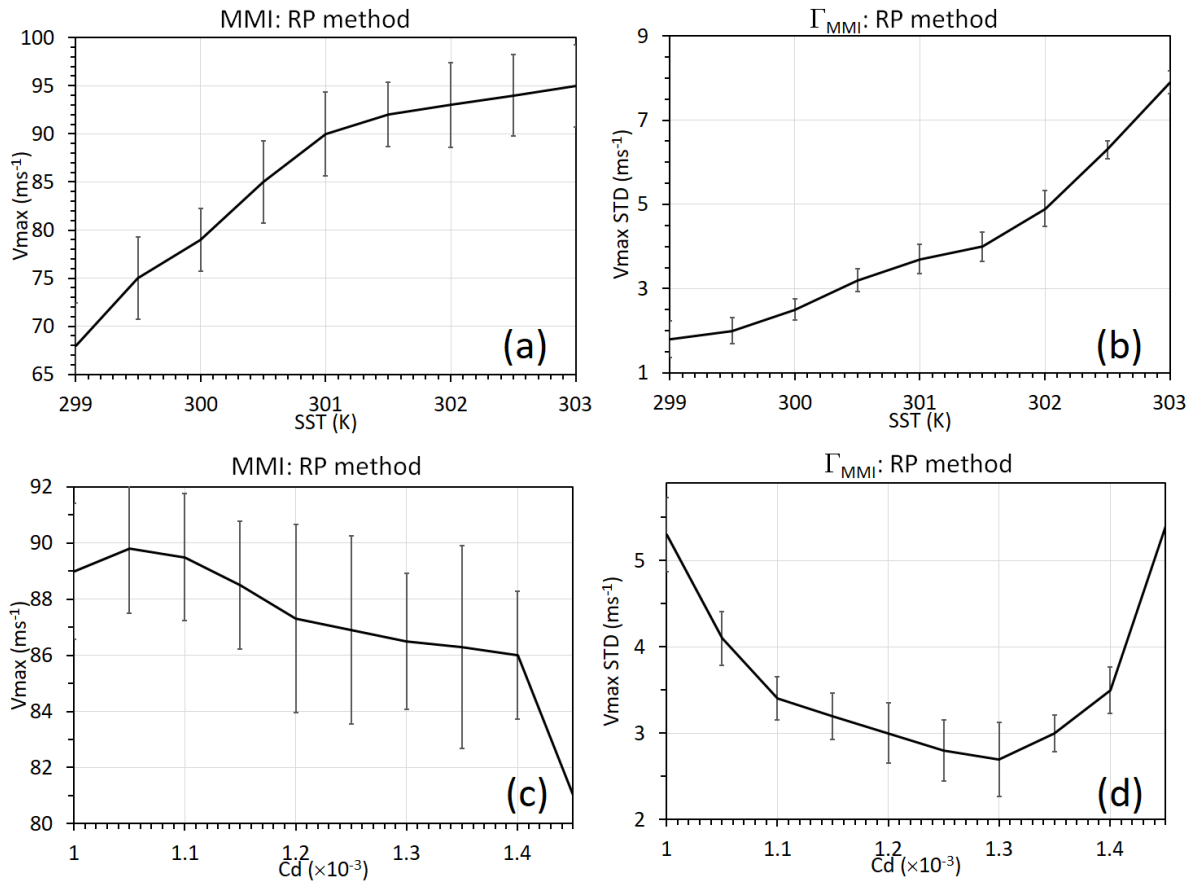


Figure 10. Dependence of V_{MAX} (left panels) and its corresponding standard deviation (right panels) on (a)-(b) SST and (c)-(d) C_d with a fixed noise amplitude in the time-varying RP method.

490 conditions, which capture no change in Γ_{MMI} as seen in Figure 11a. Such resilience of the intensity
 491 variability at the MMI equilibrium for both the RIC and RP methods reflects the fact that this equilibrium
 492 is not a point-like equilibrium as in the MSD model, but it may contain a chaotic attractor of TC dynamics
 493 that randomizing model parameters or initial conditions does not help. As a consequence, the fluctuation of
 494 MMI at the equilibrium is no longer linearly dependent on the random fluctuation of initial conditions or
 495 model parameters as in the MSD system. In this regard, the CM1 results shown in Figure 11 imply that
 496 long-term intensity errors in full-physics models may be subject to less of an impact caused by vortex
 497 initialization uncertainties or random model parameters/truncation errors, as compared to the intrinsic
 498 variability of TC dynamics (see, e.g., Du et al. (2013); Kieu et al. (2021)).

499 **4.2 Intensity error growth**

500 Along with the intensity error saturation, it is important to also validate the characteristics of the intensity
 501 error growth obtained from the MSD model. Unlike the MSD model in which one can add random noise
 502 for any representation method in studying error growth, the CM1 model has strong constraints on the
 503 model design and numerical stability that prevent one from adding random noise arbitrarily. Therefore, we
 504 examine in this section the error growth in the CM1 model only for the RF and RIC methods.

505 Figure 12a shows the error growth rate for the RF method obtained from the CM1 model between 48-180
 506 hrs into integration (cf. Figure 9). For this RF method, the CM1 error growth rate confirms what obtained
 507 from the MSD model, with a larger error growth rate during rapid intensification and a much slower growth

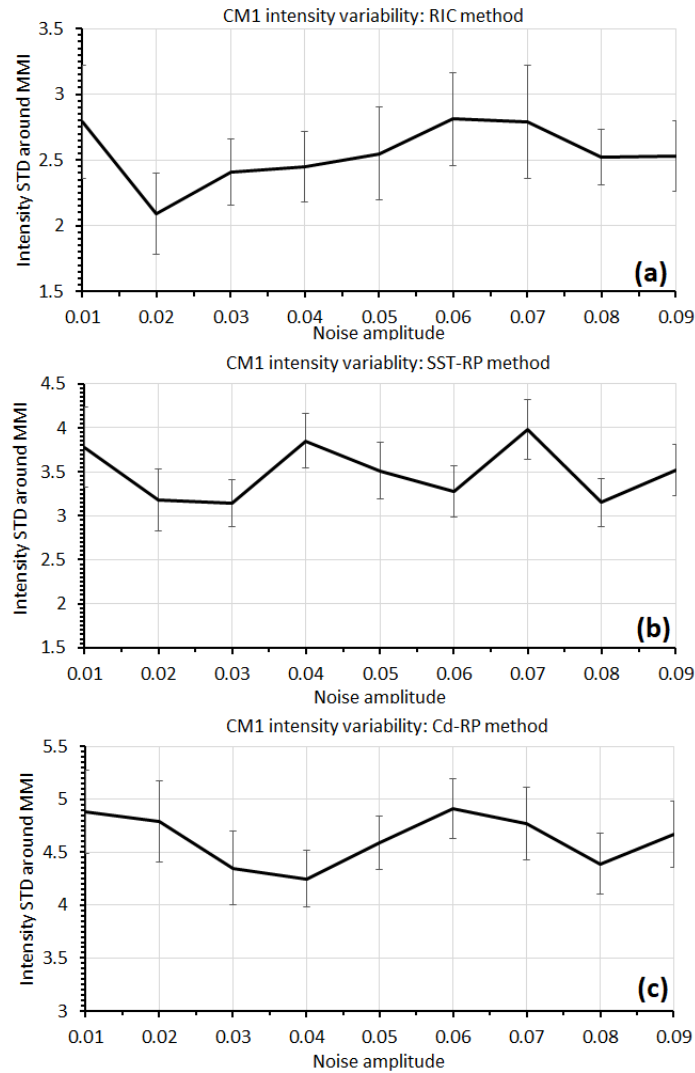


Figure 11. Similar to Figure 9b but for (a) the RIC method, (b) the initial RP method with a random SST parameter, and (c) the initial RP method with a random C_d parameter obtained from the CM1 model.

508 during the quasi-stationary stage. Detailed comparison of Figures 9 and 12 shows that the peak in the
 509 error growth rate occurs, however, around $t = 72hr$ in the CM1 model, which is after the onset of TC
 510 rapid intensification, whereas the maximum error growth in the MSD model is prior to the onset of rapid
 511 intensification (cf. Figure 7). Although this behavior of error growth in the CM1 model is difficult to be
 512 explained due to the more complex nature of TC nonlinear dynamics, it could reflect the fact that the onset
 513 of TC rapid intensification in full-physics model is generally less well-defined than that in the MSD model
 514 in the presence of stochastic forcing. Thus, any perturbation introduced into the model may be smoothed
 515 out until the model vortex enters its rapid intensification period. Of course, this is more or less a speculation
 516 at this point, because there is no effective way to isolate the smoothing effect in the CM1 model. However,
 517 it highlights some difficulty when analyzing error growth in full-physics models such as CM1, which is
 518 absent in the MSD model.

519 In contrast to the RF method, the error growth in the RIC method captures somewhat more consistent
 520 growth rate characteristics as compared to the MSD model, with the largest growth rate prior to the onset
 521 of rapid intensification (Figure 12b). Moreover, the growth rate also subsides over time, and becomes

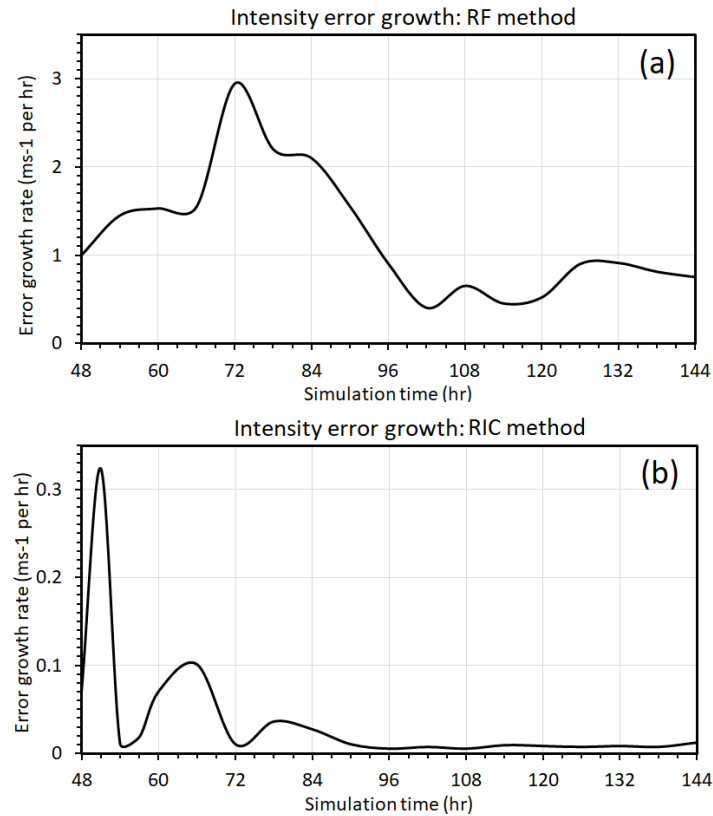


Figure 12. (a) Dependence of the error growth rate (unit ms^{-1} per hr) on the stage of TC development for the 12-hr lead time obtained from the RF implementation for the CM1 model; and (b) Similar to (a) but for the RIC implementation.

522 stabilized during the MMI stage. This result also accords with the idealized experiments and real-time
 523 intensity verification presented in Kieu et al. (2018); Keshavamurthy and Kieu (2021), thus supporting
 524 i) larger uncertainty of intensity forecast during TC rapid intensification, and ii) the existence of chaotic
 525 attractor at the MMI stage.

526 It should be noted again that the implementation of the RIC method in the CM1 model, by design,
 527 does not include stochastic forcing as in the RF method. Thus, the error growth in the RIC experiments
 528 with either the CM1 or the MSD model is resulted merely from the spread of perturbations under the TC
 529 deterministic dynamics, which possesses more well-defined onset of rapid intensification as compared to
 530 the RF implementation. In this regard, the intensity error growth in the RIC experiment shown in Figure 11
 531 could truly reflect the behaviors of intensity variability related to the initial condition uncertainty prior to,
 532 during, and after TC rapid intensification, similar to the TC dynamics in the MSD model.

5 CONCLUSIONS

533 In this study, different methods to represent stochastic processes in TC development were examined, using
 534 a fidelity-reduced TC model and a full-physics model. With the focuses on TC intensity variability at the
 535 equilibrium and the intensity error growth during TC rapid intensification, a number of significant results
 536 have been obtained from both the theoretical and numerical perspectives.

537 First, our series of Monte-Carlo simulations for the fidelity-reduced model based on the TC-scale
538 dynamics (MSD) showed that the random forcing method in which the model forcing is augmented by a
539 stochastic term results in the largest fluctuation of TC intensity at the maximum potential intensity (MPI)
540 limit as compared to randomizing either initial conditions or model parameters. In addition, the response of
541 TC intensity to the random forcing method increases with the random noise amplitude, and it is dominated
542 by the tangential wind and warm core anomaly components as reported in NKF.

543 Second, similar response of TC intensity variability to random noise was observed for the random
544 parameter method, but the response depends sensitively to how one randomizes model parameters. For
545 the initial random parameter approach in which the model parameters are randomized only at the initial
546 time, TC intensity variability at the MPI limit increases almost linearly with the noise amplitude. For the
547 time-varying random parameter method in which the model parameters are randomized every time step, the
548 intensity fluctuation is however one order of magnitude smaller as compared to initial random parameter
549 method. Such behaviors of TC intensity variability at the MPI limit are consistent with those obtained from
550 stochastic linear models and reveal the importance of how one implements random model parameters in
551 TC models.

552 Regarding the intensity error growth during TC development, it was found that the error growth rate in
553 the MSD model peaks right before the onset of rapid intensification and then gradually subsides during
554 the intensification period before leveling off at the MPI equilibrium. This characteristic of TC intensity
555 error growth was captured for all random representation methods, except for the initial random parameter
556 methods with two specific parameters T_s (sea surface temperature) and C_d (the surface drag coefficient) due
557 to their unique role in the MPI equilibrium. As such, the random variation of these two parameters produces
558 an overall larger intensity error growth rate at the MPI limit, which is not applied to other parameters or
559 random methods.

560 Third, to verify the results obtained from the fidelity-reduced MSD model, cloud-resolving simulations
561 with the CM1 model were then conducted. By implementing the same random representation methods for
562 the CM1 axisymmetric configuration, it was confirmed that random forcing plays the most significant role
563 in the variability of TC intensity as well as the intensity error growth during TC development. The CM1
564 model experiments also confirmed that random initial condition tends to be more effective during the early
565 stage of TC development but becomes less significant relative to either the random parameter or random
566 forcing method at the later stage of TC development. The findings obtained from both the MSD and CM1
567 models highlight the importance of choosing a proper random forcing method to represent the variability
568 of TC intensity in operation.

569 Two major differences between the MSD and the CM1 model that could strongly affect the analyses of
570 TC intensity variability should be noted here. First, unlike the MSD model that contains a single stable
571 MPI point with no chaos, CM1 appears to possess some classical chaotic behaviors at the MPI equilibrium
572 similar to other full-physics models (see, e.g., Kieu and Moon, 2016; Keshavamurthy and Kieu, 2021,
573 NKF). While the existence of this chaotic MPI attractor is still elusive, its potential existence is needed to
574 explain the larger intensity variability in the CM1 model, even in the absence of all stochastic forcings.
575 The results shown in Figure 11 may therefore display the variability of TC intensity due mostly to chaotic
576 dynamics rather than purely random noise as discussed in NKF. The relative contribution between chaotic
577 and stochastic variability is unknown at present, as the CM1 model does not allow for large random noise
578 amplitudes.

579 The second difference between MSD and CM1 is that the maximum intensity equilibrium in CM1 is
580 sensitive to model configuration and physical parameterizations that may or may not be maintained during
581 arbitrarily long simulation. Unlike the low-order MSD model for which a fixed environment is always
582 assumed, CM1 simulates a TC vortex in a finite domain. Without proper physical schemes such as radiative
583 parameterization or lateral boundary condition adjustment, the model domain will be eventually affected
584 by the subsidence warming in the outer region, thus changing TC environment and cause the model to
585 spin down. In this regard, the analyses of TC intensity at the maximum intensity equilibrium contain some
586 uncertainty that one has to resolve in the future studies before more definite conclusion of intrinsic TC
587 intensity variability can be obtained.

APPENDIX 1: SENSITIVITY ANALYSIS

588 The equilibrium of the MSD system (1)-(3) can be obtained by solving the following equations

$$pv_*^2 - (p + 1)b_* - c_d u_* v_* = 0 \tag{8}$$

$$-u_* v_* - c_d v_*^2 = 0 \tag{9}$$

$$b_* u_* + s u_* + T_s v_* - r b_* = 0, \tag{10}$$

589 where (u_*, v_*, b_*) denotes the critical points. From (9), $u_* = -c_d v_*$, substituting it into (10) results in

$$b_* = \frac{(T_s - s c_d) v_*}{r + c_d v_*}.$$

Now putting these into (8), we obtain

$$(p + c_d^2) v_* = (p + 1) \frac{T_s - s c_d}{r + c_d v_*}$$

$$v_* (r + c_d v_*) = \frac{(p + 1)(T_s - s c_d)}{(p + c_d^2)}$$

$$v_* = \frac{-r + \sqrt{r^2 + 4c_d K}}{2c_d}$$

590 where $K = \frac{(p+1)(T_s - s c_d)}{(p + c_d^2)} = 0.9$. Note that in order that $v_* > 0$, we must have $T_s > s c_d$.

591 The sensitivity of the critical points on model parameters can now be derived by examining the following
592 partial derivatives

$$\frac{\partial v_*}{\partial s} = \frac{-(p + 1)c_d}{(p + c_d^2)\sqrt{r^2 + 4c_d K}} \quad \text{and} \quad \frac{\partial v_*}{\partial T_s} = \frac{(p + 1)}{(p + c_d^2)\sqrt{r^2 + 4c_d K}}$$

593 and

$$\frac{\partial v_*}{\partial c_d} = \frac{r - \sqrt{r^2 + 4c_d K}}{2c_d^2} + \frac{1}{2c_d} \left(\frac{2K + 2c_d \left(\frac{-s(p+1)}{(p+c_d^2)} - \frac{2c_d(p+1)(T_s - s c_d)}{(p+c_d^2)^2} \right)}{\sqrt{r^2 + 4c_d K}} \right).$$

594 Use the typical scales for TCs including $p = 200, r = 0.25, s = 0.1, T_s = 1.0, C_d = 1.0$, we can evaluate
595 the magnitude for all of these derivatives, which then give

$$\delta v_* \approx -0.5225 \delta s \quad \text{and} \quad \delta v_* \approx 0.5225 \delta T_s. \quad \text{and} \quad \delta v_* \approx 0.120 \delta c_d. \tag{11}$$

596 For the static stability parameter s , the δs is of the order 0.01, but for the other two parameters C_d
597 and T_s , their fluctuation δT_s and δC_d are of the order 0.1 (10% of their values). Comparing these
598 variations apparently shows that δv_* is largest and thus producing the most intensity errors. Note that p is
599 relatively large while s is small as compared to other model parameters. Thus, $\frac{T_s c_d^2}{p + c_d^2} \approx 0, \frac{p}{p + c_d^2} \approx 1$, and
600 $\frac{s c_d}{\sqrt{r^2 + 4c_d(T_s - s c_d)}} \approx 0$. As a result, the relative sensitivity of intensity variation among the three parameters
601 T_s, C_d , and s is held true for a wide range of TC scales.

APPENDIX 2. LARGE-TIME BEHAVIORS OF THE VARIANCE OF AN 1-DIMENSIONAL MODEL

602 To gain some analytical insight about the effect of random parameters on dynamical systems, here we
 603 consider an idealised 1-dimensional model

$$\frac{dx(t)}{dt} = F^{\theta, \mu}(x(t)), \tag{12}$$

604 where θ and μ are parameters of the model, and the forcing function $F^{\theta, \mu}$ is real-valued. Specifically,
 605 we suppose $\theta = (\theta_t)_{t \geq 0}$ and $\mu = (\mu_t)_{t \geq 0}$ are both time-varying and random, and we consider the
 606 time-in-homogeneous system

$$\frac{dx(t)}{dt} = \theta_t(\mu_t - x(t)). \tag{13}$$

607 Intuitively, if $\theta_t > 0$ and $\mu_t = \mu_0$ for all $t \geq 0$, then μ_0 is an internal equilibrium and $x(t) \rightarrow \mu_0$ as $t \rightarrow \infty$,
 608 reminiscent to the long time behavior of the MSD system (1)-(3). Henceforth we make the following
 609 assumptions for θ :

$$\int_0^t \theta_r dr \rightarrow \infty \quad \text{as } t \rightarrow \infty \quad \text{with probability one.} \tag{14}$$

610 This mild assumption holds, for instance, when θ_t is a positive constant for all t , or an ergodic process with
 611 a positive mean value.

Solving (13) by integrating factor $I(t) = \exp \int_0^t \theta_s ds$,

$$\begin{aligned} x'(t) + \theta_t x(t) &= \theta_t \mu_t \\ [I(t)x(t)]' &= I(t) \theta_t \mu_t \\ x(t) &= \frac{1}{I(t)} \left(x(0) + \int_0^t I(s) \theta_s \mu_s ds \right) \\ x(t) &= x(0) e^{-\Theta(t)} + S_t \end{aligned} \tag{15}$$

where we wrote $\Theta(t) := \int_0^t \theta_r dr$ for simplicity, and we let

$$S_t = e^{-\Theta(t)} \int_0^t e^{\Theta(s)} \theta_s \mu_s ds.$$

612 The first term $x(0) e^{-\Theta(t)}$ on the right of (15) tends to zero exponentially fast as $t \rightarrow \infty$, by assumption
 613 (14).

614 As we shall see below, despite the simplicity of system (13), the long-time behavior of S_t (hence also that
 615 of $x(t)$) can be very different for different forms of the random trajectories $(\theta_t, \mu_t)_{t \geq 0}$, even if the mean
 616 and the variance are constant over time.

617 Scenario I: Vanishing long-time variance.

618 **EXAMPLE 1 (Vanishing variance for constant equilibrium).** Suppose $\mu_t = \mu_0 \in (0, \infty)$ for all $t \geq 0$
 619 and assumption (14) holds for θ . Then $\lim_{t \rightarrow \infty} x(t) = \mu_0$ almost surely and the variance of $x(t)$ tends to
 620 0 as $t \rightarrow \infty$. To see this, the second term on the right of (15) is $S_t = \mu_0(1 - e^{-\Theta(t)}) \rightarrow \mu_0$ and whose
 621 variance tends to 0 as $t \rightarrow \infty$.

622 EXAMPLE 2 (Vanishing variance for white noise parameters). Suppose $(\mu_t)_{t \geq 0}$ is a white noise with
 623 constant mean μ_0 and variance $\sigma^2 \in (0, \infty)$. That is, $\mu_t = \mu_0 + \sigma \eta_t$ where η_t is a standard white
 624 noise. Suppose $(\theta_t)_{t \geq 0}$ is independent with $(\mu_t)_{t \geq 0}$ and satisfies assumption (14). Then the expectation
 625 $\mathbb{E}[x(t)] \rightarrow \mu_0$ as $t \rightarrow \infty$ and the variance of $x(t)$ tends to 0 as $t \rightarrow \infty$.

To see these, note that the mean of S_t is

$$\mathbb{E}[S_t] = \mu_0 \mathbb{E} \left[\int_0^t e^{\Theta(s) - \Theta(t)} \theta_s ds \right] = \mu_0 \mathbb{E} \left[1 - e^{-\Theta(t)} \right] \rightarrow \mu_0$$

as $t \rightarrow \infty$ by assumption (14). The variance of S_t is zero for all time $t \geq 0$, because

$$\begin{aligned} \text{Var}(S_t) &= \mathbb{E} \left[\left(\int_0^t e^{\Theta(s) - \Theta(t)} \theta_s (\mu_s - \mu_0) ds \right)^2 \right] \\ &= 2 \mathbb{E} \left[e^{-2\Theta(t)} \int_{r=0}^t \int_{s=0}^r e^{\Theta(s) + \Theta(r)} \theta_s \theta_r (\mu_s - \mu_0) (\mu_r - \mu_0) ds dr \right] \end{aligned} \tag{16}$$

626 which is zero since the covariance $\mathbb{E}[(\mu_s - \mu_0) (\mu_r - \mu_0)] = 0$ for $s < r$.

627 The two examples above assert that the variance of $x(t)$ is asymptotically zero for large time, if the
 628 parameters are white noises, or if the equilibrium is very stable. In practice, one often discretizes time in
 629 simulation studies, so the parameters cannot be white noise in the strict sense and the long time variance of
 630 the system may not be exactly 0 (although as the discretization time-step $h \rightarrow 0$, the variance of S_t would
 631 tend to 0). The next two examples below show that the variance of $x(t)$ can sustain if the parameters are
 632 correlated at different times.

633 **Scenario II: Sustainable long-time variance.**

634 EXAMPLE 3 (Sustainable variance for non-white-noise parameters). The setting is the same as in
 635 Example 2, except that we replace μ by its time-discretised version $\mu^{(h)} = (\mu_t^{(h)})_{t \geq 0}$ with step-size
 636 $h \in (0, 1)$. That is, $\mu_t^{(h)} = \mu_{ih}$ for $t \in [ih, (i + 1)h)$, $i \in \mathbb{Z}_+$. In this case, the variance of S_t in (15) is
 637 well-approximated by $h\sigma^2$ as $t \rightarrow \infty$ and $h \rightarrow 0$, by (16). Hence as the discretization time-step $h \rightarrow 0$, the
 638 variance of S_t is of order h .

639 EXAMPLE 4 (Sustainable variance for OU parameters). Suppose $\theta_t = \theta_0 \in (0, \infty)$ for all $t \geq 0$, and μ_t
 640 is the Ornstein–Uhlenbeck (OU) process with mean μ_0 , that is,

$$d\mu_t = \frac{1}{2}(\mu_0 - \mu_t) dt + \sigma dW_t,$$

641 where W is a 1-dimensional Wiener process. Then the expectation $\mathbb{E}[x(t)] \rightarrow \mu_0$ and the variance of $x(t)$
 642 tends to $2\sigma^2/3$ as $t \rightarrow \infty$.

To see this, note that for all $t \geq 0$, $S_t = e^{-\theta_0 t} \int_0^t e^{\theta_0 s} \theta_0 \mu_s ds$ in (15) has mean μ_0 and variance

$$e^{-2\theta_0 t} \mathbb{E} \left[\left(\int_0^t e^{\theta_0 s} (\mu_s - \mu_0) ds \right)^2 \right] = 2 e^{-2\theta_0 t} \mathbb{E} \left[\int_{r=0}^t \int_{s=0}^r e^{\theta_0(s+r)} (\mu_s - \mu_0) (\mu_r - \mu_0) ds dr \right].$$

Since $Cov(\mu_s, \mu_t) = \sigma^2 \left(e^{-\frac{|t-s|}{2}} - e^{-\frac{(t+s)}{2}} \right)$, the variance (4) is equal to

$$\begin{aligned}
 & 2 e^{-2t} \sigma^2 \int_{r=0}^t \int_{s=0}^r e^{s+r} \left(e^{-\frac{(r-s)}{2}} - e^{-\frac{(r+s)}{2}} \right) ds dr \\
 &= 2\sigma^2 e^{-2t} \int_{r=0}^t e^{\frac{r}{2}} \int_{s=0}^r e^{\frac{3s}{2}} - e^{\frac{s}{2}} ds dr \\
 &= 2\sigma^2 e^{-2t} \int_{r=0}^t e^{\frac{r}{2}} \left(\frac{2}{3} (e^{\frac{3r}{2}} - 1) - 2(e^{\frac{r}{2}} - 1) \right) dr \\
 &= 2\sigma^2 e^{-2t} \int_{r=0}^t \frac{2}{3} (e^{2r} - e^{\frac{r}{2}}) - 2(e^r - e^{\frac{r}{2}}) dr \\
 &= \sigma^2 \left(\frac{2}{3} + C_1 e^{-t} + C_2 e^{-\frac{3t}{2}} + C_3 e^{-2t} \right) \\
 &\rightarrow \frac{2\sigma^2}{3} \quad \text{as } t \rightarrow \infty.
 \end{aligned}$$

643 We expect the above simple examples are generic, as similar behavior of system variance in terms of
 644 random parameters is also demonstrated in other complex dynamical systems. For instance, in Fan et al.
 645 (2021a), incompressible 3D fluid flows subject to a shear induced by OU movement of the boundary were
 646 examined, which confirmed that the variance of the energy dissipation rate is of the same order as that of
 647 the OU process.

ACKNOWLEDGMENTS

648 This research was partially supported by ONR Awards N000141812588. CK wishes to thank the NOAA
 649 Geophysical Fluid Dynamics Laboratory and Princeton University for their support and hospitality during
 650 the sabbatical period that this work was prepared. We wish to also thank two anonymous reviewers for
 651 their suggestions and comments, which have helped improve this work.

AUTHOR CONTRIBUTIONS STATEMENT

652 CK perceived the idea and designed experiments. LF carried out mathematical analyses. MP performed
 653 simulations and analyses. All authors contributed to the writing of the manuscript.

DATA AVAILABILITY STATEMENT

654 This study requires no dataset. All details of the model, initial condition, and parameters are provided in
 655 the Methodology section.

REFERENCES

656 Aberson, S. D., Aksoy, A., Sellwood, K. J., Vukicevic, T., and Zhang, X. (2015). Assimilation of
 657 high-resolution tropical cyclone observations with an ensemble kalman filter using hedas: Evaluation of
 658 2008–11 HWRF forecasts. *Mon. Wea. Rev.* 143, 511–523

- 659 Aksoy, A., Aberson, S. D., Vukicevic, T., Sellwood, K. J., Lorsolo, S., and Zhang, X. (2013). Assimilation
660 of high-resolution tropical cyclone observations with an ensemble kalman filter using noaa/aoml/hrd's
661 hedas: Evaluation of the 2008–11 vortex-scale analyses. *Mon. Wea. Rev.* 141, 1842–1865
- 662 Arakawa, A. and Schubert, W. H. (1974). Interaction of a cumulus cloud ensemble with the large-scale
663 environment, part i. *Journal of Atmospheric Sciences* 31, 674 – 701. doi:10.1175/1520-0469(1974)
664 031<0674:IOACCE>2.0.CO;2
- 665 Breil, M. and Schädler, G. (2017). Quantification of the uncertainties in soil and vegetation
666 parameterizations for regional climate simulations in europe. *Journal of Hydrometeorology* 18, 1535 –
667 1548. doi:10.1175/JHM-D-16-0226.1
- 668 Brown, B. R. and Hakim, G. J. (2013). Variability and predictability of a three-dimensional hurricane in
669 statistical equilibrium. *J. Atmos. Sci.* 70, 1806–1820. doi:10.1175/JAS-D-12-0112.1
- 670 Bryan, G. H. and Fritsch, J. M. (2002). A benchmark simulation for moist nonhydrostatic numerical
671 models. *Mon. Wea. Rev.* 130, 2917–2928
- 672 Christensen, H., Moroz, I., and Palmer, T. (2015). Stochastic and perturbed parameter representations of
673 model uncertainty in convection parameterization. *J. Atmos. Sci.* 72, 2525–2544
- 674 Christensen, H. M. (2020). Constraining stochastic parametrisation schemes using high-resolution
675 simulations. *Quarterly Journal of the Royal Meteorological Society* 146, 938–962. doi:10.1002/qj.3717
- 676 Doblus-Reyes, F. (2009). Addressing model uncertainty in seasonal and annual dynamical ensemble
677 forecasts. *Quart. J. Roy. Meteor. Soc.* 135, 1538–1559
- 678 Dorrestijn, J., Crommelin, D., A.P. Siebesma, H. J., and Jakob, C. (2015). Stochastic parameterization of
679 convective area fractions with a multicloud model inferred from observational data. *J. Atmos. Sci.* 72,
680 854–869
- 681 Du, T. D., Ngo-Duc, T., Hoang, M. T., and Kieu, C. Q. (2013). A study of connection between tropical
682 cyclone track and intensity errors in the wrf model. *Meteor. Atmos. Phys.* 122, 55–64. doi:10.1007/
683 s00703-013-0278-0
- 684 Fan, W.-T. L., Jolly, M., and Pakzad, A. (2021a). Three-dimensional shear driven turbulence with noise at
685 the boundary. *Nonlinearity* 34, 4764
- 686 Fan, W.-T. L., Kieu, C., Sakellariou, D., and Patra, M. (2021b). Hitting time of rapid intensification onset
687 in hurricane-like vortices. *Physics of Fluids* 33, 096603. doi:10.1063/5.0062119
- 688 Gopalakrishnan, S. G., Marks, F., Zhang, X., Bao, J.-W., Yeh, K.-S., and Atlas, R. (2011). The experimental
689 HWRF system: A study on the influence of horizontal resolution on the structure and intensity changes
690 in tropical cyclones using an idealized framework. *Mon. Wea. Rev.* 139, 1762–1784
- 691 Hakim, G. J. (2011). The mean state of axisymmetric hurricanes in statistical equilibrium. *Journal of the*
692 *Atmospheric Sciences* 68, 1364–1376. doi:10.1175/2010jas3644.1
- 693 Halperin, D. J. and Torn, R. D. (2018). Diagnosing conditions associated with large intensity forecast
694 errors in the hurricane weather research and forecasting (HWRF) model. *Weather and Forecasting* 33,
695 239 – 266. doi:10.1175/WAF-D-17-0077.1
- 696 Hamill, T. M., Whitaker, J. S., Kleist, D. T., Fiorino, M., and Benjamin, S. G. (2011). Predictions of 2010's
697 tropical cyclones using the gfs and ensemble-based data assimilation methods. *Mon. Wea. Rev.* 139,
698 3243–3247
- 699 Kain, J. S. and Fritsch, J. M. (1990). A one-dimensional entraining/detraining plume model and its
700 application in convective parameterization. *Journal of Atmospheric Sciences* 47, 2784 – 2802. doi:10.
701 1175/1520-0469(1990)047<2784:AODEPM>2.0.CO;2

- 702 Keshavamurthy, K. and Kieu, C. (2021). Dependence of tropical cyclone intrinsic intensity variability on
703 the large-scale environment. *Quarterly Journal of the Royal Meteorological Society* 147, 1606–1625.
704 doi:<https://doi.org/10.1002/qj.3984>
- 705 Kieu, C. (2015). Hurricane maximum potential intensity equilibrium. *Quarterly Journal of the Royal*
706 *Meteorological Society* 141, 2471–2480
- 707 Kieu, C., Evans, C., Jin, Y., Doyle, J. D., Jin, H., and Moskaitis, J. (2021). Track dependence of tropical
708 cyclone intensity forecast errors in the COAMPS-TC model. *Weather and Forecasting* 36, 469–485
- 709 Kieu, C., Keshavamurthy, K., Tallapragada, V., Gopalakrishnan, S., and Trahan, S. (2018). On the growth
710 of intensity forecast errors in the operational hurricane weather research and forecasting (HWRf) model.
711 *Q. J. R. Meteorol. Soc.* 144, 1803–1819
- 712 Kieu, C. Q. and Moon, Z. (2016). Hurricane Intensity Predictability. *Bull. Amer. Meteor. Soc.* doi:10.1175/
713 BAMS-D-15-00168.1
- 714 Kieu, C. Q. and Wang, Q. (2017). Stability of tropical cyclone equilibrium. *J. Atmos. Sci.* 74, 3591–3608
- 715 Kieu, C. Q. and Wang, Q. (2018). On the scale dynamics of the tropical cyclone intensity. *Discrete and*
716 *Continuous Dynamical Systems - B* 23, 3047
- 717 Kurihara, Y., Bender, M. A., Tuleya, R. E., and Ross, R. J. (1995). Improvements in the GFDL hurricane
718 prediction system. *Monthly Weather Review* 123, 2791–2801
- 719 Liu, Q., Marchok, T., Pan, H., Bender, M., and Lord, S. (2000). Improvements in hurricane
720 initialization and forecasting at ncep with global and regional (GFDL) models. *Procedures Bull.*
721 *472, NCEP/EMC. [Available from NOAA/NWS, 1325 East–West Highway, Silver Spring, MD 20910 at*
722 *<http://205.156.54.206/om/tpb/472.htm>*
- 723 Nguyen, P., Kieu, C., and Fan, W.-T. L. (2020). Stochastic variability of tropical cyclone intensity at the
724 maximum potential intensity equilibrium. *Journal of the Atmospheric Sciences* 77, 3105–3118
- 725 Palmer, T. N. (2001). A nonlinear dynamical perspective on model error: A proposal for non-local
726 stochastic–dynamic parametrization in weather and climate prediction models. *Quart. J. Roy. Meteor.*
727 *Soc* 127, 279–304
- 728 Palmer, T. N. (2012). Towards the probabilistic earth-system simulator: A vision for the future of climate
729 and weather prediction. *Quart. J. Roy. Meteor. Soc.* 138, 841–861
- 730 Plant, R. and Craig, G. C. (2008). A stochastic parameterization for deep convection based on equilibrium
731 statistics. *J. Atmos. Sci.* 65, 87–105
- 732 Rappin, E. D., Nolan, D. S., and Majumdar, S. J. (2013). A highly configurable vortex initialization method
733 for tropical cyclones. *Monthly Weather Review* 141, 3556 – 3575. doi:10.1175/MWR-D-12-00266.1
- 734 Richter, D. H., Wainwright, C., Stern, D. P., Bryan, G. H., and Chavas, D. (2021). Potential low bias
735 in high-wind drag coefficient inferred from dropsonde data in hurricanes. *Journal of the Atmospheric*
736 *Sciences* 78, 2339 – 2352. doi:10.1175/JAS-D-20-0390.1
- 737 Song, Y., Wikle, C. K., Anderson, C. J., and Lack, S. A. (2007). Bayesian estimation of stochastic
738 parameterizations in a numerical weather forecasting model. *Monthly Weather Review* 135, 4045 – 4059.
739 doi:10.1175/2007MWR1928.1
- 740 Sugihara, G., Grenfell, B. T., May, R. M., and Tong, H. (1994). Nonlinear forecasting for the classification
741 of natural time series. *Philosophical Transactions of the Royal Society of London. Series A: Physical*
742 *and Engineering Sciences* 348, 477–495. doi:10.1098/rsta.1994.0106
- 743 Suhas, E. and Zhang, G. J. (2014). Evaluation of trigger functions for convective parameterization schemes
744 using observations. *Journal of Climate* 20, 7647–7666

- 745 Tallapragada, V., Bernardet, L., Gopalakrishnan, S., Kwon, Y., Liu, Q., Marchok, T., et al. (2012). Hurricane
746 Weather Research and Forecasting (HWRF) model: 2012 scientific documentation. *Developmental*
747 *Testbed Center* 99
- 748 Tong, M., Sippel, J. A., Tallapragada, V., Liu, E., Kieu, C., Kwon, I.-H., et al. (2018). Impact of assimilating
749 aircraft reconnaissance observations on tropical cyclone initialization and prediction using operational
750 HWRF and GSI ensemble–variational hybrid data assimilation. *Monthly Weather Review* 146, 4155 –
751 4177. doi:10.1175/MWR-D-17-0380.1
- 752 Trabing, B. C. and Bell, M. M. (2020). Understanding error distributions of hurricane intensity forecasts
753 during rapid intensity changes. *Weather and Forecasting* 35, 2219 – 2234. doi:10.1175/WAF-D-19-0253.
754 1
- 755 Van Nguyen, H. and Chen, Y.-L. (2011). High-resolution initialization and simulations of typhoon morakot
756 (2009). *Monthly weather review* 139, 1463–1491
- 757 Weisheimer, A., Palmer, T. N., and Doblas-Reyes, F. J. (2011). Assessment of representations of
758 model uncertainty in monthly and seasonal forecast ensembles. *Geophysical Research Letters* 38.
759 doi:10.1029/2011GL048123
- 760 Zhang, F. and Weng, Y. (2015). Predicting hurricane intensity and associated hazards: A five-year real-time
761 forecast experiment with assimilation of airborne doppler radar observations. *Bull. Amer. Meteor. Soc.*
762 96, 25–33
- 763 Zhang, J. (2010). Estimation of dissipative heating using low-level in situ aircraft observations in the
764 hurricane boundary layer. *J. Atmos. Sci* 67, 1853–1862
- 765 Zhang, J. A., Marks, F. D., Montgomery, M. T., and Lorsolo, S. (2010). An estimation of turbulent
766 characteristics in the low-level region of intense hurricanes allen (1980) and hugo (1989). *Monthly*
767 *Weather Review* 139, 1447 – 1462. doi:10.1175/2010MWR3435.1
- 768 Zhang, Z., Tallapragada, V., Kieu, C., Trahan, S., and Wang, W. (2015). HWRF based ensemble prediction
769 system using perturbations from GEFS and stochastic convective trigger function. *Tropical Cyclone*
770 *Research and Review* 3, 145–161
- 771 Zou, X. and Tian, X. (2018). Hurricane warm-core retrievals from amsu-a and remapped atms measurements
772 with rain contamination eliminated. *Journal of Geophysical Research: Atmospheres* 123, 10,815–10,829.
773 doi:https://doi.org/10.1029/2018JD028934